PCCP
Physical Chemistry Chemical Physics

Accepted Manuscript

This article can be cited before page numbers have been issued, to do this please use: V. Raji, I. Stojkovi Simatovi, L. Veselinovi, J. Beloševi avor, M. Novakovi, M. Popovi, S. Skapin, M. Mojovic, S. Stojadinovic, V. Rac, I. Jankovi-astvan and S. Markovi, *Phys. Chem. Chem. Phys.*, 2020, DOI: 10.1039/D0CP03377D.

ROYAL SOCIETY OF CHEMISTRY

rsc.li/pccp

View Article Online
DOI: 10.1039/D0CP03377D

ARTICLE

Bifunctional catalytic activity of $Zn_{1-x}Fe_xO$ toward OER/ORR: Seeking an optimal stoichiometry

Received 00th January 20xx,
Accepted 00th January 20xx

DOI: 10.1039/x0xx00000x

Vladimir Rajić,[a] Ivana Stojković Simatović,[b] Ljiljana Veselinović,[c] Jelena Belošević Čavor,[a] Mirjana Novaković,[a] Maja Popović,[a] Srečo Davor Škapin,[d] Miloš Mojović,[b] Stevan Stojadinović,[e] Vladislav Rac,[f] Ivona Janković Častvan[g] and Smilja Marković*[c]

Eco-friendly and rapid microwave processing of a precipitate was used to produce Fe-doped zinc oxide ($Zn_{1-x}Fe_xO$, x=0, 0.05, 0.1, 0.15 and 0.20; ZnO:Fe) nanoparticles, which were tested as catalysts toward the oxygen reduction reaction (ORR) and oxygen evolution reaction (OER) in a moderately alkaline solution. The phase composition, crystal structure, morphology, textural properties, surface chemistry, optical properties and band structure were examined to comprehend the influence of Zn^{2+} partial substitution with Fe^{3+} on the catalytic activity of ZnO:Fe. Linear sweep voltammetry showed an improved catalytic activity of ZnO:5Fe toward ORR, compared to pure ZnO, while with increased amounts of the Fe-dopant the activity decreased. The improvement was suggested by a more positive onset potential (0.394 V *vs*. RHE), current density (0.231 mA·cm^{-2} at 0.150 V *vs*. RHE), and faster kinetics (Tafel slope, b = 248 mV·dec^{-1}), and it may be due to the synergistic effect of (1) a sufficient amount of surface oxygen vacancies, and (2) a certain amount of plate-like particles composed of crystallites with well developed (0001) and (000$\bar{1}$) facets. Quite the contrary, the OER study showed that the introduction of Fe^{3+} ions into the ZnO crystal structure resulted in an enhanced catalytic activity of all ZnO:Fe samples, compared to pure ZnO, probably due to the modified binding energy and an optimized band structure. With the maximal current density of 1.066 mA·cm^{-2} at 2.216 V *vs*. RHE, the onset potential of 1.856 V *vs*. RHE, and the smallest potential difference between OER and ORR (ΔE=1.58 V), ZnO:10Fe may be considered a promising bifunctional catalysts toward OER/ORR in moderately alkaline solution. This study demonstrates that the electrocatalytic activity of ZnO:Fe strongly depends on defect chemistry and consequently band structure. Along with providing a fundamental insight into the electrocatalytic activity of ZnO:Fe, the study also indicates an optimal stoichiometry for an enhanced bifunctional activity toward OER/ORR, compared to pure ZnO.

Introduction

In 21st century, when an energy crisis and environmental pollutions arises as one of the major global problems, scientific and engineering community worldwide made many effort to develop advanced systems efficient to generate clean energy through photo/electrochemical water splitting, regenerative fuel cells and rechargeable metal–air batteries.[1–6]

Oxygen reduction reaction (ORR) and oxygen evolution reaction (OER) have been recognized as the two main reactions involved in fuel cells and metal–air batteries.[1,4,7] The ORR take place during discharging, oxidizing the metal at the counter electrode, while the OER occurs during charging, oxidizing the metal at the counter electrode.[4,8] ORR involves numerous consecutive steps, including oxygen diffusion from the atmosphere to the catalyst surface, oxygen adsorption on the catalyst surface, and electron transfer from the anode to the oxygen molecules on the cathode surface to form the discharge product.[9] To be highly efficient, energy storage devices, or metal–air batteries required fast ORR, also, highly-reversible to regenerate oxygen molecules during the charging process where OER takes place. The main problems of both ORR and OER, such as sluggish kinetics, high overpotential and poor reversibility of oxygen chemistry, can be overcame by using catalysts. Until now, Pt is the best electrochemical ORR catalysts, while RuO_2 and IrO_2 are the best OER catalysts.[1] However, the limiting factors for noble metals are high cost, and low activity toward OER, while catalysts containing ruthenium or iridium were shown to be promising for OER only, also, suffer from limited stability.[9] That is why the development of bifunctional catalysts, equally active toward both ORR and OER, becomes imperative for energy conversion technologies since they might reduce the production costs and simplify the manufacturing process.[9,10]

Until now, various types of nanostructured materials have been tested as bifunctional catalysts toward OER/ORR, such as: spinels,[4,11,12] perovskites,[4,7] sulphides and selenides,[13] nitrides,[14] phosphorene,[15] carbon materials,[16] metals, and their composites.[4,17] Various studies have been reported about efficient activities of single or mixed metal oxides toward

[a] University of Belgrade, Vinča Institute of Nuclear Sciences, Belgrade, Serbia.
[b] University of Belgrade, Faculty of Physical Chemistry, Belgrade, Serbia.
[c] Institute of Technical Sciences of SASA, Belgrade, Serbia.
Email: smilja.markovic@itn.sanu.ac.rs
[d] Jožef Stefan Institute, Ljubljana, Slovenia.
[e] University of Belgrade, Faculty of Physics, Belgrade, Serbia.
[f] University of Belgrade, Faculty of Agriculture, Zemun, Serbia.
[g] University of Belgrade, Faculty of Technology and Metallurgy, Belgrade, Serbia.

OER/ORR.[4,10,18–20] Besides, transition-metal oxides based on ZnO were revealed as active catalysts toward ORR or OER.[21,22] Actually, zinc oxide-based materials can offer great possibilities as catalysts. Attractiveness of ZnO is attributed to wide-bandgap energy at room temperature (3.37 eV), large exciton binding energy (60 meV), high electron mobility and transfer efficiency (115–155 $cm^2 \cdot V^{-1} \cdot s^{-1}$), intrinsic stability, non-toxicity, environmental compatibility, as well as to simple and inexpensive synthesis procedure. Catalytic activity of ZnO-based material, can be easily tuned by: (1) metal and nonmetal ion doping, (2) hydrogenation, (3) the incorporation of crystalline defects in the form of vacancies and interstitials, (4) the modification of particles morphology and surface topology, etc.[23] We found that microwave processed ZnO-based particles exhibit enhanced photo(electro)catalytic properties. That is explained by a very rich defect chemistry incited by rapid crystallization driven by microwave irradiation.[24] As well, photo(electro)catalytic properties can be additionally improved by tuning surface-to-bulk defect ratio.[25]

In our previous paper we presented a detailed study about effects of Zn^{2+} partial substitution with Fe^{3+} on the local structure, hyperfine interaction and magnetic properties of $Zn_{1-x}Fe_xO$ nanoparticles ($0 \leq x \leq 0.2$), where XRD and TEM results were used as an illustrative support.[26] The goal of the present study is to examine their electrocatalytic activity, and we have found that $Zn_{1-x}Fe_xO$ nanoparticles exhibit improved bifunctional activities toward OER and ORR in a moderately alkaline electrolyte solution (pH = 8). Seeking to comprehend the influence of Fe^{3+} to Zn^{2+} partial substitution in the ZnO host on the catalytic activity of ZnO:Fe samples, we have systematically investigated decisive features, such as crystal structure, morphology, textural properties, surface chemistry, optical properties and band-structure. The functional properties are correlated with physicochemical characteristics and the origin of the catalytic activity was discussed.

Experimental

Materials and synthesis of catalysts

Zinc chloride ($ZnCl_2$, purity > 99.5, Lach-Ner, Neratovice, Czech Republic) and iron (III) chloride hexahydrate ($FeCl_3 \times 6H_2O$, Acros Organics, Geel, Belgium) were used as zinc and iron sources, respectively; sodium hydroxide (NaOH, purity > 98%, Carlo Erba Reagents) was used as a precipitating agent. All chemicals were used directly as received from the manufacturers without additional purification. Distilled water was used as the solvent and for powder rinsing, while absolute ethanol (Lach-Ner, Neratovice, Czech Republic) was used for the final rinsing.

ZnO powders with nominally 0, 5, 10, 15 and 20 at.% of iron were prepared by microwave processing of a precipitate. Appropriate amounts (listed in Table 1) of $ZnCl_2$ and $FeCl_3 \times 6H_2O$ were dissolved in 100 ml of distilled water. In the following step, an amount of 20 mL of 1.75 M NaOH was added dropwise to the solution of zinc and iron sources with continuous stirring for about 20 min. After being stirred at 50 °C for 90 min in total, the as-prepared white precipitate was microwave processed in a domestic oven (2.45 GHz, 130 W) for 5 min. After cooling to room temperature, the suspension was centrifuged at 5000 rpm for 10 min, rinsed five times with distilled water and successively with absolute ethanol to remove the surface residual of the starting chemical solutions. Synthesized powders were air dried in an oven at 60 °C for 24 h.

Throughout this paper, the synthesized powders are designated as ZnO, ZnO:5Fe, ZnO:10Fe, ZnO:15Fe, and ZnO:20Fe. The numbers denote nominal Fe^{3+} amount (in at. %) substituting Zn^{2+} in the ZnO crystal structure; 5, 10, 15 and 20, respectively.

Characterization of catalysts

The zinc and iron contents in ZnO were determined by an inductively coupled plasma spectrometer coupled with optical emission spectroscopy (ICP-OES, Spectro Arcos). Before the analysis samples were diluted in concentrated HCl. The crystal structure and phase purity of the catalysts were investigated by X-ray diffraction using a Philips PW-1050 with Cu $K\alpha_{1,2}$ radiation (40 kV, 20 mA). The data were collected over a 2θ range 10–90° with a step of 0.05° and a counting time of 5 s per step. The crystal phases were identified by comparing the recorded data with those reported in the International Centre for Diffraction Data (ICDD) database. The unit cell parameters were calculated by the LSUCRI computing program using the least-squares method.[27] The crystallite sizes (D) were calculated from XRD line-broadening using the Scherrer equation.[28] The intrinsic defects and distortions in the ZnO crystal structure with an increased Fe amount were studied by Raman spectroscopy. The room-temperature μ-Raman spectra were collected in the frequency interval of 50–1500 cm^{-1} (DXR Raman microscope, Thermo Scientific) with a resolution of 4 cm^{-1}. The 532 nm line of a diode-pumped solid-state high-brightness laser was used as the excitation source. The surface functional groups of the catalysts were analysed using Fourier transform infrared (FT–IR) spectra recorded on a Thermo Scientific™ Nicolet™ iS™10 FT–IR Spectrometer equipped with an attenuated total reflectance (ATR) accessory. ATR/FT–IR measurements were done in the wavenumber region of 400–4000 cm^{-1}, with a resolution of 4 cm^{-1}. X-ray photoelectron spectroscopy (XPS) measurements were carried out to clarify the surface element composition and the valence state of the oxygen and iron ions in the ZnO:Fe catalysts. XPS measurements were carried out using the SPECS system with a monochromatic source of X-radiation (Al K_α line with a photon energy of 1486.3 eV). Survey spectra were recorded in the FAT40 mode with step energy of 0.5 eV, and the acquisition time of 0.2 s/channel. The high-resolution spectra of the main photoelectron lines for Zn, Fe, and O were recorded in the FAT20 mode with the step energy of 0.1 eV, and the acquisition time of 2 s/channel. The pressure in the analysis chamber was kept at 10^{-8} mbar during the measurements. The XPS analysis was done on the as-received powders; the powder was pressed onto a copper double-sided adhesive tape to provide mechanical support and electrical contact. Despite this, there was the effect of surface charging, common for non-conductive samples. As a direct consequence of surface charging, a shift of all lines towards higher energies occurred indicating that the surface was positively charged. Therefore, the binding energies were corrected using the position of C 1s peak located at 284.8 eV (for adventitious carbon originating from impurities due to exposure to air) for calibration. The EPR spectra were recorded at room temperature

View Article Online DOI: 10.1039/D0CP03719G

using Bruker Elexsys II E540 EPR spectrometer operating at X-band (9.51 GHz). For low temperature EPR measurements, the samples were inserted into quartz EPR cuvettes (Wilmad-Lab Glass, USA). The cuvettes were frozen in cold isopentane for the EPR measurements at 19 K using a Bruker Elexsys-II spectrometer with an Oxford Instruments ER 4112HV helium cryostat. In both cases, the experimental conditions were included modulation amplitude of 5 G, modulation frequency 100 kHz, and microwave power 10 mW. The spectra were recorded using the Xepr software (Bruker BioSpin) and analysed by the ELEANA computer program. To investigate the distribution of Fe ions in ZnO:Fe particles, high-angle annular dark field scanning transmission electron microscopy (HAADF-STEM) and energy-dispersive X-ray fluorescence spectroscopy (EDX) with elemental maps were performed using TEM (FEI, Talos F200X) operated at 200 keV. The samples for TEM investigation were prepared by dispersing the ZnO:Fe powder in ethanol, after dispersion a drop of the solution was placed on a carbon-coated copper grid and dried in air. The particles morphology was characterized by field emission scanning electron microscopy (FE–SEM). The samples for the FE–SEM analysis were dispersed in water, in an ultrasonic bath (at a frequency of 40 kHz and power of 50 W), for 30 min; after dispersion a few drops were filtered through a cellulose acetate membrane. The membrane was put on a carbon tape on the aluminum stub and carbon-coated for electron reflection. Before the analysis, the sample was vacuumed for 15 min. The recorded FE-SEM micrographs were used to estimate the average particle size by measuring the diameters of more than 250 particles with a SemAfore digital slow scan image recording system (version 4.01 demo; JEOL, Tokyo, Japan). The specific surface area (SSA) and the distribution of pores were determined based on a N_2 adsorption–desorption isotherm at –195.8 °C using an ASAP 2020 (Micromeritics Instrument Corporation, Norcross, GA, USA). Prior to analysis, the samples were degassed under reduced pressure at 120 °C for 10 h. The SSA was calculated according to the Brunauer–Emmett–Teller (BET) method from the linear part of the N_2 adsorption isotherm.[29] The total pore volume (V_{total}) was estimated from the adsorbed amount at the relative pressure of p/p_0 = 0.998. The volume of mesopores (V_{meso}) and the pore size distribution were analysed according to the Barrett–Joyner–Halenda (BJH) method from the desorption branch of the isotherm.[30] The volume of micropores (V_{micro}) was calculated from the alpha-S plot. Optical properties were studied by UV–Vis diffuse reflectance (DRS) and photoluminescence (PL) spectroscopy. The UV–Vis DRS were collected using an Agilent Cary 5000 spectrophotometer equipped with a diffuse reflectance accessory. The measurements were performed in the 800–200 nm region, with a 1 nm data interval and 600 nm/min scan rate, using a commercial PTFE standard for baseline correction. The PL spectra were recorded on a Horiba Jobin Yvon Fluorolog FL3–22 spectrofluorometer using Xe lamp excitation.

Electrochemical activity of catalysts

The electrocatalytic (EC) activity of the ZnO:Fe samples was explored using linear sweep voltammetry (LSV). The EC measurements were performed on a Gamry PCI4/750 using a conventional three-electrode cell and an aqueous solution of 0.1M Na_2SO_4 (p.a. Merck), pH ~ 8, as the electrolyte. Platinum foil and standard calomel electrode (SCE) were used as the counter and the reference electrode, respectively, while FTO glass (Sigma-Aldrich 20 $\Omega \cdot cm^{-2}$) was used as working electrode. The working electrode was coated with catalysts ink; the ink was prepared by mixing 5 mg of a zinc oxide-based powder as an active material with 10 µL 5% Nafion solution (Ion Power, USA) as a binder, 50 µL ethanol and 50 µL water. This slurry was homogenized for 45 min in an ultrasonic bath, and subsequently, an amount of 50 µL of prepared ink was coated on the working electrode as a thin film. To evaporate the solvent, the electrode was dried at room temperature for 30 min. The surface area of the working electrode was about 3 cm^2. All potentials were measured against the SCE and converted to a reversible hydrogen electrode (RHE) scale using the equation:

$$E_{RHE}\ (V) = E_{SCE} + 0.244 + 0.059\ pH \quad (1)$$

To ensure gas saturation for oxygen reduction reaction (ORR) testing, high-purity O_2 gas (99.998 %) was bubbled into the electrolyte solution for 15 min before and during the EC measurements. LSV was measured in potential range between 0.816 and −0.284 V *vs*. RHE with a scan rate of 5 $mV \cdot s^{-1}$. The overpotential (η) was defined as µ= E (vs RHE) – 0.514 V. The number of electrons transferred in the ORR process was calculated using the Koutecky-Levich equation:

$$\frac{1}{j} = \frac{1}{j_k} + \frac{1}{B\omega^{1/2}} \quad (2)$$

Parameter *B* is defined as:

$$B = 0.62nF\nu^{-1/6}C_{O_2}D_{O_2}^{2/3} = n \cdot k \quad (3)$$

where *n* is the number of electrons exchanged per molecule of O_2, *F* is the Faraday constant, *υ* is the kinematic viscosity of the electrolyte, C_{O2} is the bulk concentration of O_2 and D_{O2} is the diffusion coefficient of O_2 in 0.1 M Na_2SO_4.[1] The constant *k* was determined using a Pt ring disk as working electrode for the ORR at the same experimental conditions as for ZnO:5Fe. The value of the constant *k* was 1.238 (the number of electrons for Pt is 4). The ZnO:5Fe suspension (5µL) was loaded on the glassy carbon (GC) rotating disc electrode (RDE) which was used as working electrode (surface 0.19625 cm^2). The LSV measurements were performed in O_2 saturated 0.1 M Na_2SO_4 aqueous solution at several different rotation speeds (from 300 to 1200 rpm) by a scan rate of 5 $mV \cdot s^{-1}$ from 0.816 to −0.484 V *vs*. RHE. For oxygen evolution reaction (OER) LSV was measured with a scan rate of 5 $mV \cdot s^{-1}$ in the voltage range between 0.916 V and 2.216 V *vs*. RHE.

Photocatalytic test

The photocatalytic activity of the ZnO:Fe samples was tested by the decolorization of methylene blue (MB) dye under direct sunlight illumination. The experiments were done between 12 a.m. and 15 p.m. during the month of August 2019 and at ambient temperature (25 to 28 °C). The intensity of light was measured by a PeakTech 5165 Digital-Lux-Meter and it varied between 900 and 1000 lux. In each experiment, 100 mg of the photocatalyst was mixed with 100 mL of the MB (Methylen blay B extra, E. Merck, Darmstadt, Germany) with a concentration of 10 ppm in a beaker. To distinguish the efficiency of degradation from adsorption, prior to illumination the suspension was magnetically stirred for 1 h in dark to establish the adsorption-desorption equilibrium. After equilibrium was established, the concentration of MB was measured and taken as the initial concentration C_o. During illumination stirring was maintained to keep the mixture in suspension. At specific time intervals, 3 mL aliquots were sampled and centrifuged (5000 rpm, 5 min) to remove particles from the solution before absorbance measurements. Solution concentrations were monitored by a GBC Cintra UV–Vis spectrophotometer in the wavelength range of 450–750 nm; the concentration of MB was calculated according to the absorbance value at 665 nm.

Computational method

The calculations were performed using the (linearized) augmented plane waves + local orbitals ((L)APW+lo) method based on the density functional theory (DFT), embedded in the WIEN 2k code.[31] The volume, *c*/*a* ratio and the internal structural parameters of ZnO were optimized using the PBE-GGA[32] exchange-correlation potential, after which a 2×2×2 supercell (32 atoms) from periodically repeating ZnO unit cells was constructed. Finally one Zn atom was replaced with Fe to simulate Fe-doped ZnO. To model oxygen and zinc vacancy, one nearest neighbour oxygen and one next nearest neighbour zinc atom around Fe were removed. The Brillouin zone (BZ) integration in our calculations was done *via* a tetrahedron method,[33] using 24 k points in the irreducible wedge of the Brillouin zone, while the cut-off parameter $R_{MT}K_{max}$ for limiting the number of plane waves was chosen to be 8. In all our calculations the charge convergence criterion was employed, requesting the charge difference between the iterations to be smaller than 10^{-5} electrons. To avoid a severe underestimation of the band gap by the GGA, the band structure calculations for the obtained relaxed structures were done using modified Becke-Johnson (mBJ) exchange potential.[34] The absorption spectra were calculated from the relation:

$$\alpha(\omega) = \sqrt{2\left[\sqrt{\varepsilon_1{}^2(\omega) + \varepsilon_2{}^2(\omega)} - \varepsilon_1(\omega)\right]} \quad (4)$$

where α(ω) is the absorption coefficient, $\varepsilon_1(\omega)$ is the imaginary part of the dielectric tensor computed from the calculated band structures and $\varepsilon_2(\omega)$ is the real part of the dielectric tensor evaluated from the Kramers-Kroning relation.[35]

Results and discussion

Chemical composition

The contents (in wt.%) of zinc and iron in ZnO:Fe particles were investigated by a ICP-OES analysis, with an experimental error of 0.1 %. The results were used to calculate the number of Zn and Fe atoms (in at.% in relation to 1 atom of Zn+Fe) in the $Zn_{1-x}Fe_xO$ unit cell. The ICP-OES analysis showed that the total content of iron in the ZnO:Fe samples was 5.0, 11.7, 15.0 and 21.0 at.% for the samples ZnO:5Fe, ZnO:10Fe, ZnO:15Fe and ZnO:20Fe, respectively. The calculated stoichiometric formulae are listed in Table 1.

Phase composition and the crystal structure ordering

The XRD patterns of the Fe-substituted ZnO catalysts ($Zn_{1-x}Fe_xO$, x = 0, 0.05, 0.10, 0.15, and 0.20) are shown in Fig. 1(a). All the patterns indicate highly crystalline ZnO particles with a hexagonal wurtzite-type crystal structure, $P6_{3mc}$ space group (COD no. 96-230-0113),[36] except the ZnO:20 pattern, where low-intensity reflection was identified at 35.3° 2θ, suggesting the existence of the $ZnFe_2O_4$ spinel phase. It should be pointed out that the reflection at 35.3° 2θ is the most intensive one in XRD pattern of the cubic $ZnFe_2O_4$ spinel phase with $Fd\bar{3}m$ space group, corresponding to the (311) crystal plane (COD no. 96-230-0616).[37] The existence of a $ZnFe_2O_4$ spinel phase in the ZnO:20Fe sample is confirmed by the existence of the second most intensive reflection of $ZnFe_2O_4$ at 62° 2θ (corresponding to the (440) crystal plane) observed after the pattern deconvolution.

In order to study the effect of the Fe concentration on the crystal structure of $Zn_{1-x}Fe_xO$, various crystal parameters were calculated, including unit cell parameters (*a*, *c*) and volume (*V*), as well as the average crystallite size and crystallite sizes in three specific crystallographic directions [100], [002], and [101], associated with the polarity value, $I_{(002)}/I_{(100)}$. The calculated values are listed in Table 1. The unit cell parameters calculated for pure ZnO particles were found to be $a=b$=3.25174(1) Å, c=5.21222(2) Å, V=47.729(2) Å^3 which is in good agreement with the parameters for ZnO crystals with a wurtzite-type hexagonal structure.[36] The orientation of crystal growth was determined according to crystallite size in the crystallographic directions [100], [002] and [101] and the values were equal to 15, 14 and 13.5 nm, respectively, indicating an almost isotropic nano-crystallites growth. The calculated polarity value, $I_{(002)}/I_{(100)}$, of 0.98 indicates a well-developed terminal polar planes (0001) and (000$\bar{1}$).[25] We found that the presence of iron in the amount of 5 to 20 at.% slightly influenced the unit cell parameters and the volume of microwave processed ZnO:Fe particles comparing to those of the pure ZnO sample synthesized by the same process. The most profound effect on crystal lattice growth was observed when the percentage of substitution was adjusted to 5 at.%, while the smallest lattice parameters were calculated for the ZnO:20Fe sample, probably because a part of Fe ions were involved in formation of the $ZnFe_2O_4$ spinel phase. The crystallite sizes were also slightly influenced by the Fe^{3+} to Zn^{2+} substitution; the polarity values varied in 12% upon substitution, pointing that growth orientation was determined by the percentage of Fe^{3+} ions in the precipitate.

Presented XRD results confirm that the rapid microwave irradiation of the $(Zn(OH)_2,Fe(OH)_3)$ precipitate enabled an easy Fe^{3+} cation incorporation, up to 15 at.%, into the Zn^{2+} lattice site without distorting the crystal structure of ZnO. The absence of distortion can be explained by: (1) the similarity of the crystal radii of Fe^{3+} and Zn^{2+} (actually, in the tetragonal coordination, the crystal radius of Zn^{2+} is equal to 0.74 Å while the crystal radius of Fe^{3+} is equal to 0.63 Å);[38] (2) zinc oxide crystal structure with a network of tetrahedra formed by the oxygen atoms, is sufficiently flexible to stay stable despite the partial substitution of Zn with up to 15 at.% of Fe. The $Zn_{1-x}Fe_xO$ crystal structure, with partially substituted Zn^{2+} with Fe^{3+} has a great potential for both electrocatalytic and photocatalytic activity, due to greater contribution of charge carriers.[6]

Table 1 Experimental details, stoichiometry, unit cell parameters with standard deviations, crystallite sizes in specific crystallographic directions, average crystallite sizes, and polarity.

Sample notation	Amount of cation sources in 100 ml		Stoichiometry based on ICP	Unit cell parameters			Crystallite size, D (nm)			Average crystallite size, D_{av} (nm)	$I_{(002)}/I_{(100)}$
	$ZnCl_2$ (g)	$FeCl_3$ (g)		$a=b$ (Å)	c (Å)	V (Å^3)	D_{100}	D_{002}	D_{101}		
ZnO	0.8976	/	ZnO	3.25174(1)	5.21222(2)	47.729(3)	15	14	13.5	12.0	0.98
ZnO:5Fe	0.8631	0.0903	$Zn_{0.95}Fe_{0.05}O$	3.2525(8)	5.21336(2)	47.764(2)	15	14	13.5	11.8	1.09
ZnO:10Fe	0.8177	0.1802	$Zn_{0.88}Fe_{0.12}O$	3.2519(8)	5.21016(6)	47.716(2)	16	15	14	12.4	1.15
ZnO:15Fe	0.7723	0.2703	$Zn_{0.85}Fe_{0.15}O$	3.25173(5)	5.21178(1)	47.725(1)	14	13	12	10.3	1.07
ZnO:20Fe	0.7269	0.3604	$Zn_{0.79}Fe_{0.21}O$	3.25119(1)	5.21128(2)	47.705(2)	13	13	12	9.9	1.17

View Article Online
DOI: 10.1039/D0CP03377D

ARTICLE

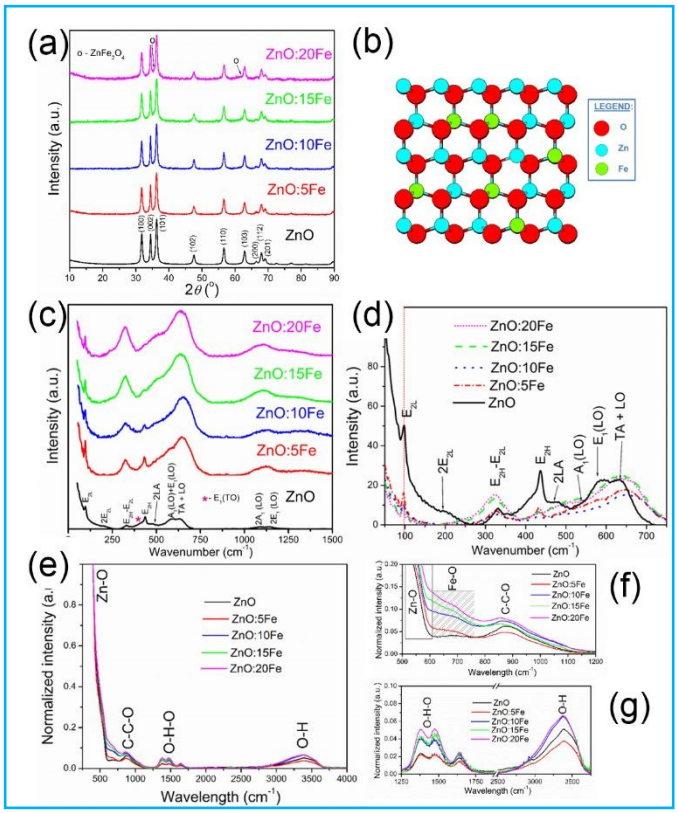

Fig. 1 (a) XRD patterns of the ZnO:Fe particles, (b) Illustration of the ZnO:Fe crystalline structure, (c) Raman spectra of ZnO:Fe particles, (d) Overlapped Raman spectra, (e) FTIR spectra of the ZnO:Fe particles, (f) expanded 500–1200, and (g) 1250–3750 cm^{-1} regions.

Raman spectroscopy is powerful tool to study change in the local structure, defect state and disorder in ZnO host lattice caused by incorporation of transition metal ions.[39] Room-temperature μ-Raman spectra of ZnO:Fe nanoparticles are shown in Figs. 1 (c–d). The most intensive band in the Raman spectrum of pure ZnO, centered at 98 cm^{-1}, corresponds to the nonpolar optical mode E_{2L}, and may be related to vibration of zinc sub-lattice.[40] A weak shoulder at 200 cm^{-1} is attributed to the second-order phonon mode $2E_{2L}$, while a small-intensity peak at 327 cm^{-1} is attributed to the zone boundary multi phonons E_{2H}-E_{2L}.[41] Another weak shoulder, at 405 cm^{-1} (marked with a pink asterisk in Fig. 1 (c)), may be ascribed to the E_1 (TO) mode. The existence of E_1 (TO) mode indicates that ZnO crystallites have propagation in a direction other than the *c*-axis typical of ZnO particles,[42] which is in accordance with nearly isotropic crystallite geometry calculated from the XRD data for three most characteristic crystallographic directions (Table 1). A sharp peak centered at 436 cm^{-1} is assigned to the E_{2H} optical mode and it is due to vibration of oxygen atoms.[41] The asymmetry of the E_{2H} peak can points to lattice disorder while its intensity indicates crystallinity;[43] thus, pure ZnO nanoparticles have a good crystallinity. A wide band in the 510–710 cm^{-1} spectral region holds two bands; the first one centered near 570 cm^{-1} is due to longitudinal optic (LO) mode consisted of A_1 (near 574 cm^{-1}) and E_1 (near 587 cm^{-1}) modes, whereas the other, at 635 cm^{-1} represents a combination of acoustic and optical modes (TA+LO). These two LO modes may be associated with the bulk defects such as oxygen vacancies, zinc interstitials or defect complexes containing both.[41] It has been shown that the presence of impurities and defects strongly influences both LO modes, especially E_1 (LO).[44] The relatively high-intensity of the A_1 (LO) + E_1 (LO) modes in the Raman spectrum of pure ZnO, Fig. 1 (c), points to certain amount of intrinsic bulk defects, caused by rapid crystallization driven by microwave irradiation.[24,25] The A_1 (LO) mode is accompanied with a low intensity wide band near 480 cm^{-1}, which is ascribed to the interfacial surface phonon mode 2LA, distinctive for surface defects.[41,45] The wide band in the wavenumber region 1090–1150 cm^{-1} is attributed to the optical overtone 2LO, namely to $2A_1$ (LO) and $2E_1$ (LO). The phonon modes observed in the Raman spectrum of pure ZnO are typical for a wurtzite ZnO with a space group of C_{6v}^4.[46] All peaks in the Raman spectra of ZnO:Fe samples can also be attributed to wurtzite ZnO, without additional peaks related to secondary phases or impurities, Fig 1 (c). As the Fe content increases, the Raman modes E_{2H}-E_{2L}, A_1 (LO)+E_1 (LO), and TA+LO, becomes broader and more intensive comparing to the bands of the high and low frequency branch of E_2 mode, as the representative peaks of wurtzite structure. Vanishing of the E_{2H} mode with increases of the Fe^{3+} content in ZnO:Fe can be correlated with increases in the lattice stress. The lattice stress is two-fold determined: (1) by charge compensation required when extra-positively charged Fe^{3+}substitute Zn^{2+}, and (2) by the lattice expansion caused by the incorporation of Fe^{3+} ions with smaller crystal radius (0.63 Å) into Zn^{2+} (0.74 Å) site in ZnO host.[47,48] As the concentration of Fe increased from 5 to 20 at. %, the E_{2H} and E_{2H}-E_{2L} optical modes were slightly red-shifted, comparing to pure ZnO sample, which is due to softening of the Zn–O bond as a result of the substitution.[49] In order to compare the Raman signal intensity, the spectra were overlapped with respect to the same intensity range, Fig. 1 (d). Lowered intensity of the E_1(LO) and 2LA modes suggest reduced density of surface and bulk defects comparing to pure ZnO. The Raman spectra provides the clue that the partial substitution of Zn^{2+} with Fe^{3+} significantly altered local ordering in ZnO, with the distressing of the symmetry of the lattice, while the crystal structure remains the same.

Surface chemistry

ATR/FT–IR spectroscopy was used to identify functional groups on the surface of ZnO:Fe particles and the changes due to Fe^{3+} to Zn^{2+} substitution. As can be seen from Fig. 1 (e), the most intensive band in the spectra of pure ZnO and ZnO:Fe is in the 400–600 cm^{-1} region and it is attributed to the Zn—O stretching vibrations in the ZnO lattice.[25] The low intensity peak centered near 870 cm^{-1} is assigned to the C—O out-of-plane bending mode.[50] The broad bands in the spectral regions 1250–1750 and 2750–3750 cm^{-1} are ascribed to the in-plane bending and stretching vibrations, respectively, of O—H groups from the adsorbed water molecule hydrogen bonded to the surface of ZnO:Fe particles.[25] From Figs. 1 (f-g), which show the expanded 500–1200 and 1250–3750 cm^{-1} regions, may be observed

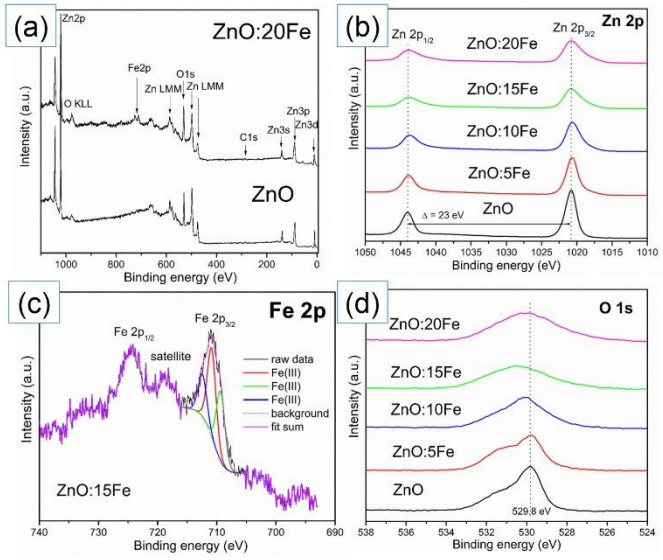

Fig. 2 (a) Full-range XPS spectra of the ZnO and ZnO:20Fe particles; High-resolution XPS spectra of: (b) Zn 2p, (c) Fe 2p of ZnO:15 Fe and (d) O 1s.

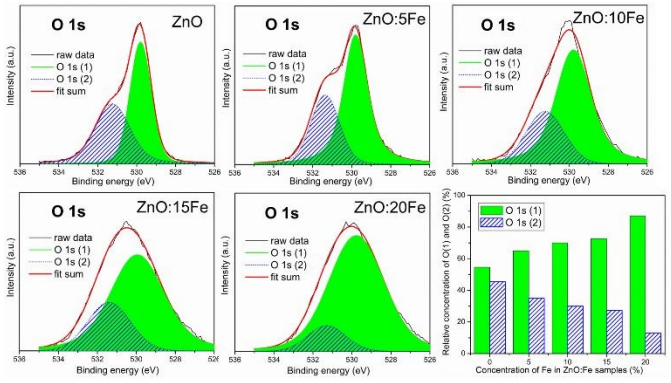

Fig. 3 High-resolution XPS spectra of O 1s peaks deconvoluted with the Voigt function, and the O 1s (1) and O 1s (2) relative amount calculated from the XPS spectra.

some changes in the FTIR spectra, compared to that of pure ZnO. First of all, the substitution of Zn^{2+} with Fe^{3+} leads to the broadening of the Zn—O stretching vibrations; the shoulder arises in the 600–750 cm^{-1} region, with an increased intensity and a slight blue shift with the increased Fe amount. The shoulder is attributed to the Fe—O stretching vibrations. Besides, the increased substitution of Zn^{2+} with Fe^{3+} in the ZnO crystal lattice leads to a larger amount of surface adsorbed hydroxyl groups - as expected, in order to maintain the overall electroneutrality. The exception to this rule in the case of ZnO:5Fe particles can be explained by the specific (plate-like) particles morphology shown in the section Morphology and textural properties.

The XPS measurement was used to further analyse the surface elemental composition and to determine the oxidation state of elements in the ZnO:Fe particles. The XPS spectra were analysed by taking the C 1s peak (284.5 eV) as the reference. Fig. 2 (a) shows the XPS survey spectra of pure ZnO and ZnO:20Fe, as the representative of the maximal concentration of iron ions. The survey confirms the presence of C, O, and Zn in both samples, while the peak (seen as a doublet due to spin-orbit splitting) at around 717 eV in the spectra of ZnO:20Fe, ascribed to Fe 2p line, is an unambiguous confirmation of Fe^{3+} to Zn^{2+} substitution in the ZnO:Fe samples.[51] The atomic concentrations of C, O, Zn, and Fe were calculated using the areas under the related peaks and the results are listed in Table 2, along with the O/(Zn+Fe) ratio. These results revealed the following correlation: the increase of the Fe content in the ZnO:Fe particles results in the simultaneous decrease of Zn and increase of O contents. The reduction in Zn amount is due to its substitution with Fe, while the amount of O increases in order to maintain the overall electroneutrality, retaining an unchanged wurtzite structure, which is in accordance with the XRD data. Besides, the zinc substoichiometry (O/Zn = 1.16) found for pure ZnO sample can be associated with a large amount of point defects produced by microwave processing.[25] The high-resolution XPS spectra were recorded to determine the binding energy positions and the spin-orbit splitting constant which are indicative of the elements' oxidation states.[22] The observed spin-orbit splitting energy of the Zn 2p peaks (23.2 eV) in the high-resolution XPS spectra, Fig. 2 (b), confirms the presence of the 2+ oxidation state of Zn in the ZnO:Fe crystal lattice.[22,52] It can be noticed that the intensities of Zn 2p lines, centered at 1020.8 and 1044 eV, gradually decreased, becoming broader and more asymmetrical (toward a lower binding energy side) with the increase of the Fe^{3+} content in the ZnO:Fe samples. This can be attributed to a decrease in the electron density at the Zn site due to the variation of the broken Zn–O bonds in the ZnO structure,[22] which provides evidence for Zn^{2+} to Fe^{3+} substitution in the ZnO:Fe samples. Fig. 2 (c) shows the high-resolution XPS spectrum of Fe 2p for the ZnO:15Fe sample, where Fe $2p_{3/2}$ and Fe $2p_{1/2}$ peaks are centered at 710.8 and 724.4 eV, respectively, accompanied with a satellite peak observed near 719 eV. The Fe $2p_{3/2}$ line can be resolved into three components centered at 709.4, 710.9 and 712.4 eV, which according to Biesinger et al.[51] belong to the Fe^{3+} state, indicating that Fe^{3+} ions substitutes Zn^{2+} in ZnO samples. The presence of the Fe^{3+} ions is additionally confirmed by EPR. The high-resolution XPS spectra of the O 1s line is shown in Fig. 2 (d). The asymmetry of the O1s peak, with a shoulder at a higher binding energy, suggests the presence of at least **two-**component O species in the ZnO sample. As can be seen, the O 1s line is strongly altered with the increase of the Fe content in the ZnO:Fe samples becoming broader. To provide more information about the type of O species, O 1s peaks were deconvoluted by two Voigt function representing O 1s (1) and O 1s (2); the deconvoluted O 1s spectra are presented in Fig. 3, while the calculated percentage of O 1s (1) and O 1s (2), as well as their ratio are listed in Table 2. Among the two deconvoluted O 1s peaks, the low-energy one, positioned at 529.8 eV (labelled as (1)) is assigned to O^{2-} ions from the Zn–O bonds in the ZnO lattice,[53] while the peak centred at 531.2 eV (labelled as (2)) is attributed to the

Table 2 Atomic composition of the ZnO:Fe samples determined by the XPS analysis.

Sample	C (at.%)	O (at.%)	Zn (at.%)	Fe (at.%)	O/(Zn+Fe)	O 1s (1) (%)	O 1s (2) (%)	O1/O2
ZnO	4.5	51.3	44.1	/	1.16	54.6	45.4	1.20
ZnO:5Fe	3.4	52.5	42.3	1.9	1.19	65.0	35.0	1.86
ZnO:10Fe	3.9	53.0	40.4	2.7	1.23	70.0	30.0	2.33
ZnO:15Fe	2.3	58.1	36.4	3.2	1.47	72.7	27.3	2.66
ZnO:20Fe	1.5	59.1	34.4	4.9	1.50	87.1	12.9	6.75

View Article Online
DOI: 10.1039/D0CP03377D

ARTICLE

surface oxygen in the oxygen-deficient regions and/or is associated with absorbed oxygen species.[54] In the literature, the O 1s (2) peak is usually related to oxygen vacancies in the ZnO lattice.[54] The results show a substantial change in the O(1)/O(2) ratio with the increase of the Fe amount suggesting that oxygen vacancy defects are suppressed by substituting Zn^{2+} with Fe^{3+} in the ZnO crystal lattice. This statement is in line with the finding of PL study.

Location of point defects (surface-to-bulk), and coordination of Fe^{3+} in the ZnO:Fe

Intrinsic point defects and impurities have strong impact on photo- and electro-catalytic efficiency of ZnO materials.[24,25] In this study, EPR spectroscopy was employed to investigate the effect of the Fe^{3+} substitution amount on the surface and bulk defects in the microwave processed ZnO:Fe nanostructured particles. Besides, the EPR results were used as complementary to XPS, to confirm the coordination environment of the Fe^{3+} in the ZnO crystal lattice. The room temperature X-band EPR spectra of ZnO:Fe samples are illustrated in Fig. 4 (a). The presence of hyperfine structure in the ZnO spectrum might be correlated with the presence of transition metal impurities and/or very low natural abundance of magnetic ^{67}Zn isotope (4.11%, spin I = 5/2).[55] The EPR spectra of Fe-substituted ZnO samples show broad signals with about two orders of magnitude higher intensity than the pure ZnO. The intensity of the EPR peak gradually increases with increased concentrations of Fe ions from 5 to 15 at.%, while the exception in the case of the ZnO:20Fe particles can be explained by the existence of a spinel phase, as confirmed by the XRD data. The broad signals without fine-line structures have been previously explained by a strong dipole-dipole interaction between the transition metal ions,[56] while some authors suggest that the contribution of unpaired electrons trapped on oxygen vacancy sites cannot be excluded.[56,57] We used the first-derivative of *g* graphs to determine the *g*-factor of the ZnO:Fe samples; the values are listed in Table 3. The determined *g*-factor of 2.0023 is equal to the free-electron value attributed to an unpaired electron trapped on an oxygen vacancy site[58] and it matches very well with the data reported for ZnO:Fe,[59] indicating that Fe^{3+} ions are in tetrahedral coordination environments within the crystal lattice of ZnO, occupying Zn^{2+} ion sites. We have found that the increase in the Fe^{3+} amount gives rise to a small quantitative variation in the *g*-factors (from 2.0023 to 2.0011). This can be explained by the facts that an increased Fe concentration in the ZnO:Fe samples simultaneously (1) decreases the density of surface oxygen vacancy sites (as suggested by XPS results), and (2) reduces the single unpaired electron density. To be unambiguous, the reduction of the single unpaired electron density is caused by the suppressed degree of covalency of Zn–O bonds due the formation of the more ionic and less covalent Fe–O bonds.

To increase the intensity of the EPR signal, while diminishing thermal effects based on the Boltzmann distribution, the EPR measurements were performed at 19 K, Fig. 4 (b), Table 3. As opposed to the room temperature X-band EPR spectra, in the low-temperature spectra, two new signals appeared at g ~ 2.1 and 4.2, along with the resonance signal at g ~ 2.00 (caused by surface defects). The resonance signal at *g* ~ 2.1 can be assigned to those Fe^{3+} ions which interact by a superexchange coupling and can be considered to be distributed in clusters, whereas the EPR signal at g ~ 4.2 is due to isolated Fe^{3+} ions predominantly positioned in a tetrahedral oxygen environment with a rhombic distortion.[60] The presented EPR results go beyond the simple validation of XPS results, that iron ions were substituted as Fe^{3+} in the Zn^{2+} tetrahedral sites; they also suggest a correlation between the concentration of Fe^{3+} in $Zn_{1-x}Fe_xO$ and the density of surface oxygen vacancies. Actually, the increase of the Fe^{3+} concentration leads to the reduction of oxygen vacancy sites, as surface defects capable to trap unpaired electrons.[61] The existence of bulk oxygen vacancies, another surface or bulk point defects, or impurities was not registered.

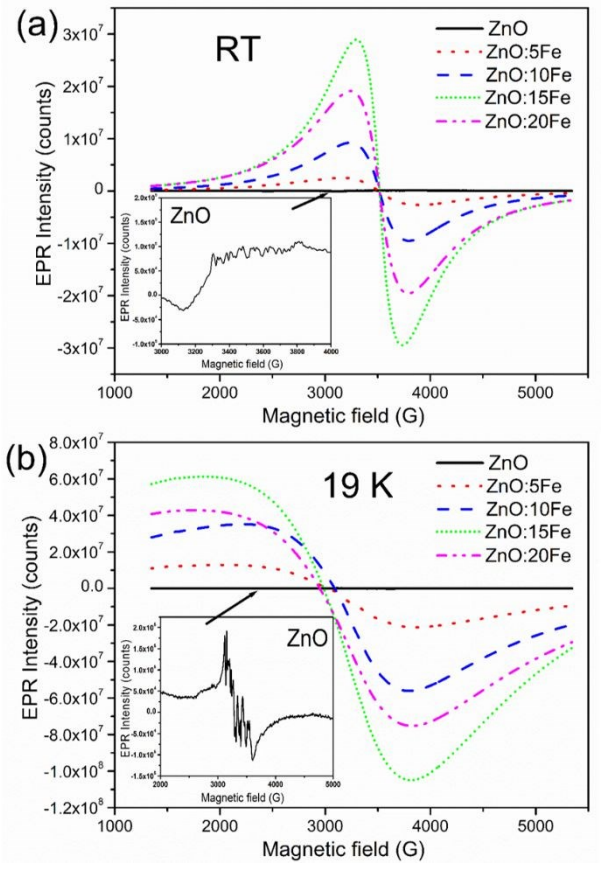

Fig. 4 (a) Room temperature X-band, and (b) 19 K EPR spectra of the ZnO:Fe samples.

View Article Online
DOI: 10.1039/D0CP03377D

ARTICLE

Table 3 Parameters estimated from the EPR, UV-Vis DRS and PL spectra.

Sample	EPR (*g* values)		DRS / E_{bg} (eV)		PL		
	RT	19 K	Dir.	Indir.	Peak	Emission	
						Violet-blue	Orange-red
ZnO	hyperfine	hyperfine	3.34	3.16	Position (nm)	415.8	627.0
					Intensity	53.5	802.7
					Area (%)	2.47	97.53
ZnO:5Fe	2.0023	1.9996 2.1081 4.2136	3.33	3.11	Position (nm) Intensity Area (%)	433.2 64.7 11.71	631.4 219.4 88.29
ZnO:10Fe	2.0021	1.9968 2.0627 4.2130	3.33	3.02	Position (nm) Intensity Area (%)	444.8 61.2 22.32	637.7 105.0 77.68
ZnO:15Fe	2.0013	1.9928 2.0646 4.2011	3.31	3.05	Position (nm) Intensity Area (%)	444.6 71.0 23.77	639.5 111.2 76.23
ZnO:20Fe	2.0011	1.9908 2.0525 4.1969	3.31	3.21	Position (nm) Intensity Area (%)	439.6 72.3 19.25	637.8 141.1 80.75

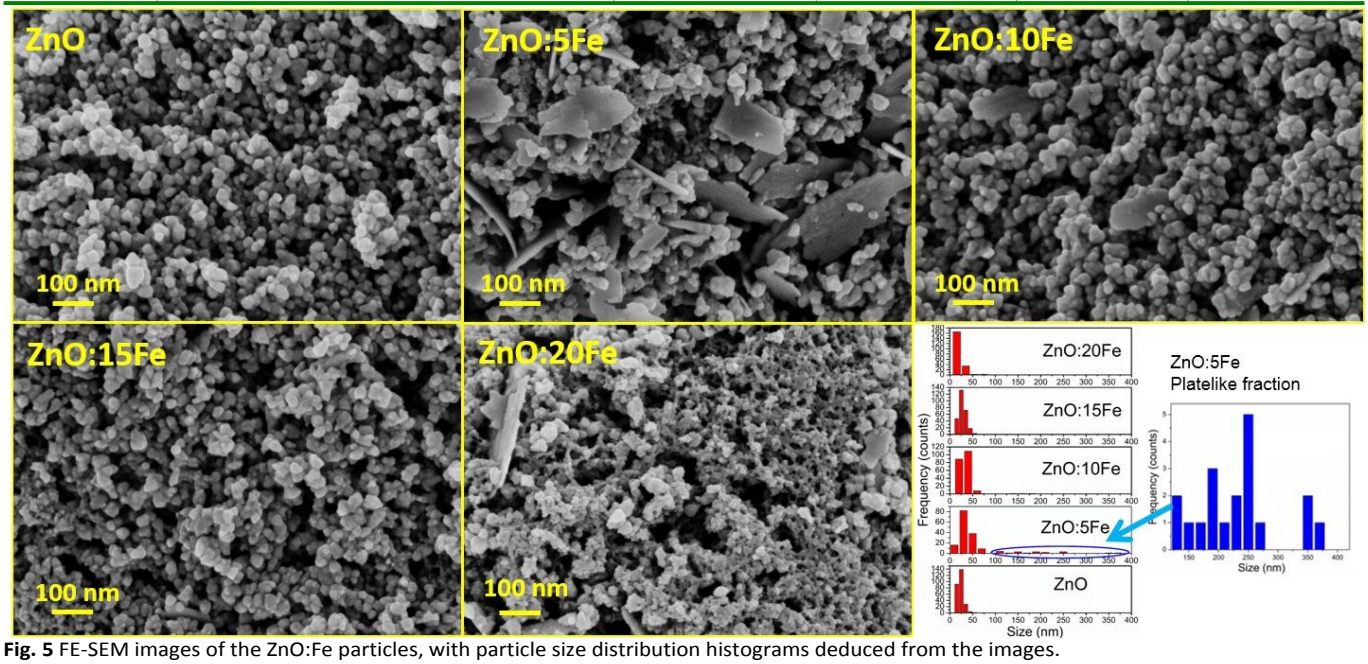

Fig. 5 FE-SEM images of the ZnO:Fe particles, with particle size distribution histograms deduced from the images.

Table 4 Effects of the Fe amount on the textural properties and morphology of the ZnO:Fe catalysts.

Sample	S_{BET} ($m^2 \cdot g^{-1}$) [a]	V_{total} ($cm^3 \cdot g^{-1}$) [b]	V_{meso} ($cm^3 \cdot g^{-1}$) [c]	V_{micro} ($cm^3 \cdot g^{-1}$) [d]	r_{av} (nm) [e]	d_m (nm) [f]	Particles shape
ZnO	36.3	0.3184	0.3184	0.0102	24.5	23	Spheroidal
ZnO:5Fe	57.2	0.2812	0.2785	0.0172	17.4	35 190	Spheroidal Platelike
ZnO:10Fe	81.1	0.3903	0.3883	0.0255	16.4	34	Spheroidal
ZnO:15Fe	88.1	0.3993	0.3962	0.0280	15.1	28	Spheroidal
ZnO:20Fe	82.4	0.3794	0.3741	0.0286	16.7	20	3D network

[a] S_{BET} – BET specific surface area; [b] V_{total} – Total pore volume; [c] V_{meso} – Volume of mesopores (2 – 50 nm); [d] V_{micro} – Volume of micropores (< 2 nm); [e] r_{av} – BJH adsorption average pore diameter; [f] d_m – mean particle size determined from FE-SEM images.

View Article Online
DOI: 10.1039/D0CP03377D

ARTICLE

Morphology and textural properties

The morphology of ZnO:Fe particles was analysed using FE-SEM. FE-SEM micrographs were also used to deduce particle size distributions employing a SemAfore digital slow scan image recording system and measuring the sample size of 250–500 particles. The representative micrographs and the corresponding particle size distribution histograms are presented in Fig. 5; the mean particle size values calculated from the histograms are listed in Table 4. The FE-SEM images reveal that all of the ZnO:Fe samples are nanocrystalline materials. The nanocrystallites of the ZnO powder are organized in spheroidal particles with a uniform size and morphology; the particles sizes vary between 10 and 50 nm, with the mean size of 23 nm. The substitution of 5 at.% Fe^{3+} for Zn^{2+} into the ZnO crystal lattice partially altered the uniformity of zinc oxide particles. Two main particle morphologies can be distinguished in the ZnO:5Fe powder, spheroidal and platelike. The spheroidal particles vary in sizes from 10 to 76 nm, with the mean size of 35 nm, while the thin platelike particles, with a smooth surface, vary in length from 100 to 365 nm and have the mean thickness of approximately 6 nm. The ZnO:10Fe powder consists of spheroidal particles with the mean size of 34 nm, while in ZnO:15Fe particles are similar to those in ZnO:10Fe but with a slightly reduced mean size of spheroidal particles to 28 nm. The morphology of the ZnO:20Fe sample is a bit different from the others, as it consists of polydispersed particles. The majority of particles are primary crystallites interconnected to form a 3D network. The crystallites sizes are estimated to range 5–15 nm, with 11 nm in average. A number of particles are spheroidal, similar to those in other ZnO:Fe samples, with sizes between 20 and 30 nm; besides, several agglomerates (up to 80 nm) and nanoplates (in length up to 320 nm) can be observed. Figure 5 demonstrates that the morphologies of the ZnO:Fe particles are somewhat modified with the Zn^{2+} to Fe^{3+} substitution in the ZnO crystal lattice. The primary particle size in the ZnO:5Fe sample are slightly larger than those in pure ZnO, while the value reduces from 35 to 20 nm with a further increase of the Fe percentage.

The FE-SEM micrographs, showing variation in the morphology of primary particles, demonstrate that the growth mechanism of ZnO:Fe particles may be considerably altered in the presence of 5 at.% of an Fe dopant despite the short time of rapid, energy-effective microwave processing. We suppose that peculiarity in the self-assembling of the ZnO:5Fe primary particles in plate-like aggregates is induced by lattice stress correlated with oxygen vacancies. [62,63] Plate-like aggregates may be observed in FESEM images of ZnO:10Fe, ZnO:15Fe and ZnO:20Fe but their number is negligibly small and decreased with decreasing of oxygen vacancies density.

The influence of Zn^{2+} to Fe^{3+} substitution on the textural characteristics of the ZnO:Fe particles was analysed by comparing a specific surface area, pore volume and pore size; the values are listed in Table 4. The specific surface area of pure ZnO particles is 36.3 m^2g^{-1}; the increase of the Fe^{3+} substitution percentage in the ZnO crystal lattice systematically increases SSA to 57.2, 81.1 and 88.1 m^2g^{-1} for ZnO:5Fe, ZnO:10Fe and ZnO:15Fe, respectively. A slight reduction of SSA in ZnO:20Fe is probably caused by the small amount of the $ZnFe_2O_4$ crystal phase. In terms of pore sizes, all ZnO:Fe materials are predominantly mesoporous (2–50 nm). The substitution of Zn with Fe slightly modifies the values of the total pore volume and the average pore diameter.

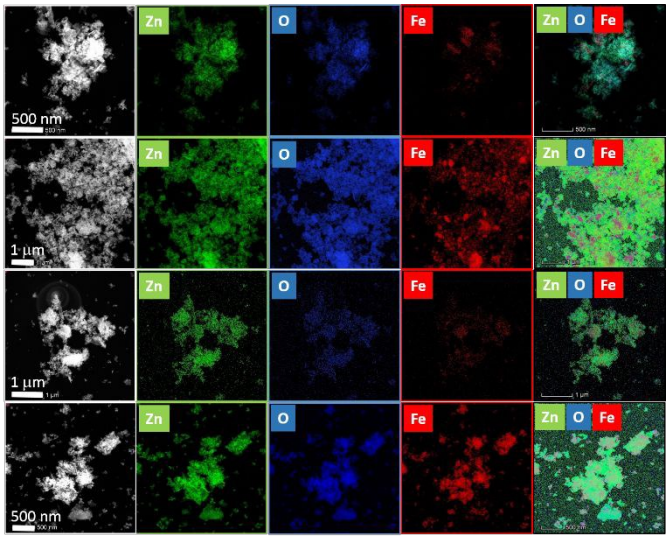

Fig. 6 HAADF-STEM images of the ZnO:Fe particles, compositional EDX maps of Zn, Fe and O and the mixed color-coded maps.

Chemical homogeneity

The fluctuation in the distribution of Zn and Fe ions in the ZnO matrix was analysed based on the high-angle annular dark-field (HAADF) imaging scanning transmission electron microscopy (STEM) images in combination with energy-dispersive X-ray fluorescence (EDX) maps of the L shell of Zn, L shell of Fe, and K shell of O. A relatively large sample area, up to 5 μm^2, was analysed to gain a better insight in elemental distribution. Fig. 6 presents HAADF-STEM images of the EDS mapping area of the ZnO:Fe particles with the mappings of Zn, O and Fe as individual elements and mixed color-coded maps. The EDS maps revealed that Zn, O and Fe ions are homogenously distributed throughout the ZnO matrix.

Optical properties

The influence of Zn^{2+} to Fe^{3+} substitution in the ZnO crystal lattice on the optical properties of the ZnO:Fe nanostructured powders was studied by UV-Vis diffuse reflectance (DR) and photoluminescence (PL) spectroscopy. As can be seen in Fig. 7 (a) the reflectance spectrum of pure ZnO was considerably altered due to a partial substitution of Zn^{2+} to Fe^{3+}. In pure ZnO the band edge absorption appears at 380 nm, stretched and shifted toward the visible region with increased Fe concentrations, suggesting the narrowing of the band gap. Furthermore, with increased Fe amounts, the percentage of absorbance significantly increases in the 380–700 nm spectral region; for example, at 450 nm the absorbance increases from 72 % for ZnO *via* 81 % for ZnO:5Fe to 93 % for ZnO:15Fe. The shape of the recorded UV-Vis DR spectra suggests the presence of additional energy levels inside the band gap. To reveal the presence of additio-

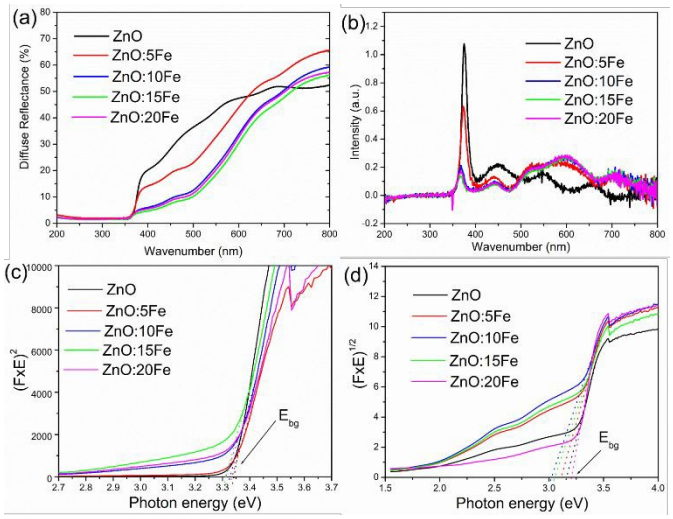

Fig. 7 (a) UV-Vis DR spectra of the ZnO:Fe samples, (b) derivative of DR spectra, (c) Kubelka–Munk plots for direct, and (d) indirect bandgap semiconductors.

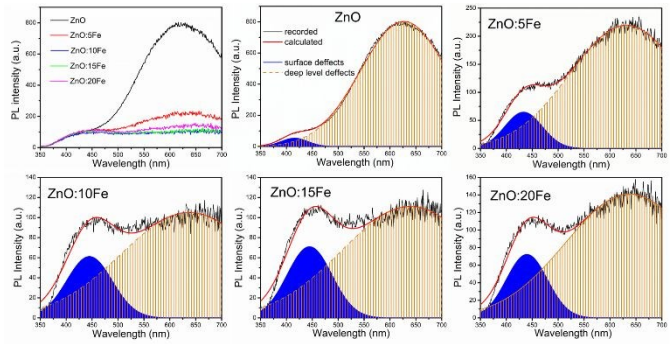

Fig. 8 Photoluminescence spectra of the ZnO:Fe samples under excitation at 280 nm, and PL spectra deconvoluted with the Gaussian function.

nal energy levels, we took the first derivative of the spectra with respect to wavelength, Fig. 7 (b). The peak at 375 nm represents the overall band gap energy while the accompanying lower energies represent additional transitions within the band gap.[64] To determine direct and indirect band gap energies (E_{bg}) of the ZnO:Fe particles, the Kubelka–Munk function was applied.[24,25] The band gap energies were estimated by extrapolating the linear part of the curves $[F(R) \times E]^2$ i.e. $[F(R) \times E]^{1/2}$ with respect to E (eV) to 0, Fig. 7 (c) and (d). The estimated values for the direct and indirect band gaps are listed in Table 3. The direct E_{bg} slightly varies from 3.34 eV for pure ZnO to 3.31 eV for ZnO:20Fe, which is in accordance with the value for bulk ZnO (3.37 eV).[65] More significant results have been found for indirect band gap energies, which values vary between 3.16 eV for ZnO and 3.02 eV for ZnO:10Fe (with the exception of two-phased ZnO:20Fe), showing a shift of the absorption edge from about 375 nm, typical for bulk ZnO, to about 410 nm, especially important for application in photocatalysis. Based on the presented UV-Vis DRS results we can conclude that the partial substitution of Zn^{2+} ions with Fe^{3+}ions in the ZnO lattice introduces new energy levels into the band gap (Fig. 7b).[66] The reduced band gap is mainly due to the presence of new energy levels below the conduction band and/or above the valence band of ZnO.[6] Due to the 3*d* orbital of Fe^{3+}, an energy level can be introduced above the valence band of ZnO, leading to a decrease in the band gap, as it will be explained in detail further in the text, part DFT calculations, Figs. 12&13. It has previously been proposed that the red shift in the band edge absorption could be caused by the *d–d* transition of Fe^{3+} or the charge transfer transition between interacting Fe^{3+} ions and due to *sp–d* exchange interaction between the band electrons and the localized *d*-electrons of Fe^{+3} ions at the Zn^{2+} site in ZnO.[6,67,68]

We used room-temperature PL spectroscopy to study the effect of Zn^{2+} to Fe^{3+} partial substitution on the surface-to-bulk defect ratio in the $Zn_{1-x}Fe_xO$ crystal lattice. The PL emission spectra of the microwave processed ZnO:Fe nanostructured samples, presented in Fig. 8, show two wide emission bands, centered near 420 and 630 nm, attributed to surface and deep-level defects, respectively.[25,69,70] The violet-blue emission near 420 nm (2.95 eV) is attributed to the transition from surface defects to the valence band (VB).[2] There is still a controversy about the origin of the violet-blue emission, it has been reported to originate from Zn_i but also from V_{Zn},[71] though that the probability of forming V_{Zn} is minor, since the enthalpy of V_{Zn} defects is higher than the enthalpy of Zn_i defects. As the XPS and EPR results suggest, only oxygen vacancies appear as surface defects in ZnO:Fe particles, we have attributed violet-blue emission to the transition from surface oxygen vacancies to the VB. The broader band in the orange-red spectral region, centered near 630 nm (1.97 eV), can be correlated to the existence of bulk oxygen vacancies; it is probably due to the transition from surface or sub-surface defects to V_O^+ or V_O^{++} in ZnO.[72,73] Fig. 8 clearly shows that the partial Fe^{3+} substitution in the ZnO:Fe samples has no significant impact on surface defects, while strongly affecting the orange-red emission band, suggesting that increased Fe concentrations in the ZnO lattice reduces the number of the bulk oxygen vacancies. As we explained in our previous papers, a large amount of intrinsic bulk defects in ZnO is due to rapid crystallization caused by the high energy delivered to the $Zn(OH)_2$ precipitate *via* microwave irradiation.[24,25] A partial substitution of the extra-positively charged Fe^{3+}, compared to Zn^{2+}, attracts more oxygen to the lattice, and consequently the incorporation of Fe^{3+} in ZnO reduces the concentration of core oxygen vacancies. For a detailed analysis of the surface-to-bulk defect ratio, the PL emission spectra were deconvoluted by two Gaussian functions, using the PeakFit software package. The deconvoluted spectra are also shown in Fig. 8, while the data obtained by deconvolution (position, intensity and area (%) of the emission bands) are listed in Table 3. The recorded PL emission spectra with additional deconvolution confirm significant effects of the Fe^{3+} concentration on the relative surface-to-bulk oxygen vacancy ratio (quantified as I_{630}/I_{430} ratio) in the ZnO:Fe particles.

Catalytic activity toward ORR and OER

During the last decade ORR and OER have been extensively studied in acidic and basic media, promoting different metal-oxides as potential electrode materials which can satisfy the requirement of current density, safety and inexpensiveness.[1,7,12] Nevertheless, we choose to test ZnO:Fe samples as electrocatalysts toward ORR and OER in moderately alkaline electrolyte, 0.1 M Na_2SO_4, with pH ~ 8. It should be pointed out that the electrochemical measurements were done on pristine ZnO:Fe powders, without mixing with carbon or any other conductive support.

Linear sweep voltammetry (LSV) study was employed to analyse the electrocatalytic activity of ZnO:Fe samples toward oxygen reduction reaction (ORR). Fig. 9 (a) shows LSV curves for the ZnO:Fe samples in 0.1 M Na_2SO_4 solution at a scan rate of 5 $mV \cdot s^{-1}$. The ORR activity of the ZnO samples was evaluated due to the potential. Actually, the onset potentials closer to the ideal value of 1.23 V *vs*. RHE indicates better electrocatalytic activity of the materials toward ORR.[22] The estimated onset potentials are find to be 0.377, 0.394,

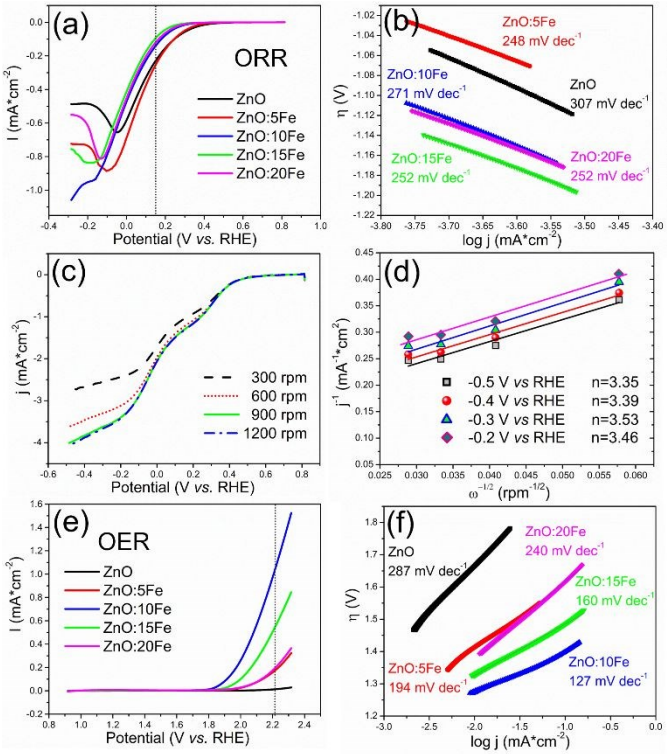

Fig. 9 (a) ORR LSVs of the ZnO:Fe electrodes in 0.1 M Na_2SO_4 solution at a scan rate of 5 mVs^{-1}, (b) Tafel plots derived from the LSVs in (a), (c) LSVs of ZnO:5Fe at a scan rate of 5 mVs^{-1}, with various rotating speeds in O_2-saturated 0.1 M Na_2SO_4, (d) Koutecky-Levich plot of ZnO:5Fe based on ORR polarization curves in (c), (e) OER LSVs of the ZnO:Fe electrodes in 0.1 M Na_2SO_4 solution at scan rate of 20 mVs^{-1}, and (f) Tafel plots derived from the LSVs in (e).

0.278, 0.228 and 0.272 *vs*. RHE for ZnO, ZnO:5Fe, ZnO:10Fe, ZnO:15Fe and ZnO:20Fe, respectively. The same activity was comprehended when current density values were compared at 0.150 V *vs*. RHE: 0.210, 0.231, 0.123, 0.080 and 0.104 $mA{\cdot}cm^{-2}$ for ZnO, ZnO:5Fe, ZnO:10Fe, ZnO:15Fe and ZnO:20Fe, respectively.

To gain better insights into the electrochemical reaction kinetics, we used Tafel plots (η *vs*. *log j*) based on the Tafel equation:

$$\eta = b \log(j/j_0) \quad (5)$$

where η is the overpotential, *b* is the Tafel slope ($mV{\cdot}dec^{-1}$), *j* is the current density, and j_0 is the exchange current density ($mA{\cdot}cm^{-2}$). Tafel plots were constructed, Fig. 9 (b), and the Tafel slopes (*b*) were determined from the linear segment in the low-potential region; the smallest *b* value point to the best catalytic activity. The Tafel slopes for ZnO, ZnO:5Fe, ZnO:10Fe, ZnO:15Fe and ZnO:20Fe were find to be 307, 248, 271, 251 and 252 $mV{\cdot}dec^{-1}$, respectively. Hence, the smallest Tafel slope of 248 $mV{\cdot}dec^{-1}$ confirmed the best electrocatalytic activity of the ZnO:5Fe toward ORR. Thus, the current density, the onset potential and the Tafel slope suggest that, compared to the pure ZnO, only the ZnO:5Fe exhibits enhanced electrocatalytic activity toward ORR, while the activity decreased for the samples with larger amount of Fe.

To go further into detail upon catalytic activity of ZnO:5Fe for ORR performance, LSV measurements were performed on a rotating disc electrode (RDE) at various rotation rates. Fig. 9 (c) shows the LSV curves of ZnO:5Fe using a GC RDE at a rotation speeds of 300–1200 rpm and a scan rate of 5 $mV{\cdot}s^{-1}$. We found that the current density gradually increased with the rotation speed. However, the LSV curve at 1200 rpm overlap with the LSV curve at 900 rpm. This can be explained as follows: total amount of oxygen in the electrolyte solution was reduced on the electrode surface at a rotation speed of

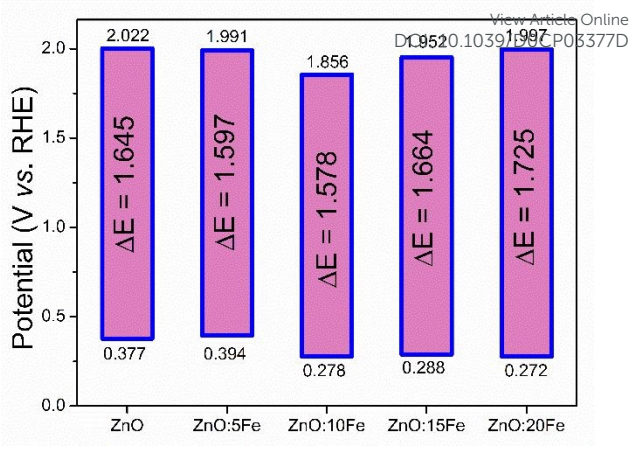

Fig. 10 Illustrative representation of the overall functionality of the ZnO:Fe catalysts.

900 rpm; thus, the maximal concentration gradient was reached and further increases of the rotation speed (1200 rpm) didn't not affected the current density. Koutecky-Levich plots (j^{-1} *vs*. $\omega^{-1/2}$) at various electrode potentials were constructed to calculate the electron transfer number (*n*) on the basis of the Koutecky-Levich (K-L) equation.[3] The Koutecky-Levich plots, presented in Fig. 9 (d), show parallel straight lines with nearly equal slope within the measured potential range which suggest the first order reaction kinetics.[3] The *n* values, calculated at potential values of -0.2, -0.3, -0.4 and -0.5 V *vs*. RHE, were found to be 3.53, 3.39 and 3.35, respectively, pointing to combined two- and four-electron pathways as further supported by appearance of two waves at polarization curves.[74]

The catalytic activity of the ZnO:Fe materials toward oxygen evolution reaction (OER) was also examined by LSV. Figure 9 (e) shows LSV curves for the ZnO:Fe samples in 0.1 M Na_2SO_4 solution at a scan rate of 5 $mV{\cdot}s^{-1}$. The current density values determined at 2.216 V *vs*. RHE were found to be 0.015, 0.171, 1.066, 0.556 and 0.202 $mA{\cdot}cm^{-2}$ for ZnO, ZnO:5Fe, ZnO:10Fe, ZnO:15Fe and ZnO:20Fe, respectively. Values of the onset potential varied as 2.022, 1.991, 1.856, 1.952 and 1.997 *vs*. RHE for ZnO, ZnO:5Fe, ZnO:10Fe, ZnO:15Fe and ZnO:20Fe, respectively. The ZnO:10Fe exhibit the lowest value of onset potentials which, in combination with the highest current density, suggest its best catalytic activity toward OER.

As for the ORR, Tafel plots were constructed, Fig. 9 (f), and the Tafel slopes (*b*) were determined from the linear segment in the low-potential region, where the smallest *b* value point to the highest catalytic activity. The determined Tafel slopes of 287, 195, 127, 160 and 240 $mV{\cdot}dec^{-1}$, correspond to the ZnO, ZnO:5Fe, ZnO:10Fe, ZnO:15Fe and ZnO:20Fe, respectively. The smallest Tafel slope of 127 $mV{\cdot}dec^{-1}$ define the ZnO:10Fe as the best catalysts for OER performance.

The overall activity of the catalyst can be validated by the potential difference (ΔE) between onset potential for OER and ORR, where the smallest ΔE point to the better reversible oxygen electrode.[1,3] Fig. 10 is illustrative representation of the potential difference for examined ZnO:Fe catalysts, where ΔE=1.58 V estimated for the ZnO:10Fe promote this material as potential bifunctional electrode materials.

Enhanced oxygen reduction reaction in the process of heterogeneous catalysis, with the ZnO:5Fe as catalysts, can be explained by the ZnO:5Fe surface chemistry and particles morphology. As we have shown, significant amount of surface oxygen vacancies and certain amount of plate-like particles characterize the ZnO:5Fe sample, which is, having in mind

mechanism of ORR in heterogeneous catalysis, beneficial to the ORR performance. Actually, the ORR in heterogeneous catalysis proceeds through adsorption of O_2 on the catalyst surface, where it must be bonded at the beginning of the reaction.[22] Thus, a good ORR catalysts should have high capability of oxygen adsorption. For that purpose, presence of surface oxygen vacancies (SOVs) in the catalysts is a necessary condition for their application in heterogeneous ORR. In fact, SOVs are the most relevant surface defects in metal-oxide particles which participate in numerous physical and chemical reactions.[75] However, since SOVs in the catalysts act as O_2 binding centers, the larger amount of SOVs provide the higher activity toward ORR. In the case of microwave processed ZnO:Fe particles, the largest amount of SOVs is detected in pure ZnO, but its catalytic activity toward ORR was not the best among ZnO:Fe. Thus, the decisive factor of improved catalytic activity of the ZnO:5Fe toward ORR may be a certain amount of plate-like particles with an average size of about 190 nm and well developed polar planes (0001) and $(000\bar{1})$. As we explained in our previous paper, the terminal polar planes (0001) and $(000\bar{1})$ should be much more active in catalysis as compared to the nonpolar facets perpendicular to them, mainly due to a higher density of defects such as oxygen vacancies.[25]

Fe dopant in ZnO enhanced its conductivity, that's why all ZnO:Fe materials have the more efficient OER activities than the pure ZnO sample. The UV-Vis DRS measurements with calculated values of indirect band gap energies (Fig. 7 (d), Table 3) show that the ZnO:10Fe has the narrower band gap (3.02 eV), suggesting the appropriate *d*-band position. This might be a reason of the higher OER activity of this material.

Photocatalysis

The influence of the Fe amount on the photocatalytic efficiency of the ZnO:Fe nanoparticles was comprehended by the degradation of a common model pollutant, methylene blue (MB), under direct sunlight illumination. Fig. 11 (a) shows the efficiency of the photocatalytic decolorization of MB dye without a catalyst (as a blank test) and in the presence of the ZnO:Fe catalysts under direct sunlight illumination. After a three-hour exposure to direct sunlight, without catalysts, degradation of MB was equal to 13.7%. The results show that between 0.6 and 2.4% of MB was adsorbed on the ZnO:Fe particles after the equilibration of the dye-photocatalyst suspension in a dark during 1 h. When sunlight was used as the illumination source, the ZnO:Fe samples showed an improved activity, compared to pure ZnO. The percent of the decolorization efficiency after 180 min of sunlight illumination increased in the following manner 47 < 61 < 67.3 < 68.8 < 100 for ZnO < ZnO:15Fe < ZnO:20Fe < ZnO:10Fe < ZnO:5Fe, respectively. Fig. 11 (b) reveals the linear kinetic curves of the $\ln(C/C_o)$ versus the illumination time graph, implicating first order reaction kinetics. The calculated kinetic parameters, the rate constant of photo-decolorization, K_1 (min^{-1}), and the time necessary for the decolorization of 50% of the dye, $t_{1/2}$ (min), are listed in Table 5. All ZnO:Fe samples show a higher decolorization efficiency than pure ZnO, whereas the ZnO:5Fe samples showed the highest efficiency, 100% after 3 h with $t_{1/2}$ about 31 min. Since all the ZnO:Fe samples have similar crystallinity and the average crystallite size, as well as the band gap energy, what's more, samples with 10, 15 and 20 at.% of Fe have a larger specific surface area and a better absorption capacity than ZnO:5Fe, the question is why the samples with Zn to Fe substitution above 5 at.% show a lower photocatalytic efficiency than ZnO:5Fe. This finding may be explained by a specific particles morphology and the surface-to-bulk oxygen vacancy ratio of the ZnO:5Fe sample. Actually, while all the other samples possess spheroidal particles of 20–35 nm in average, ZnO:5Fe is consisted of

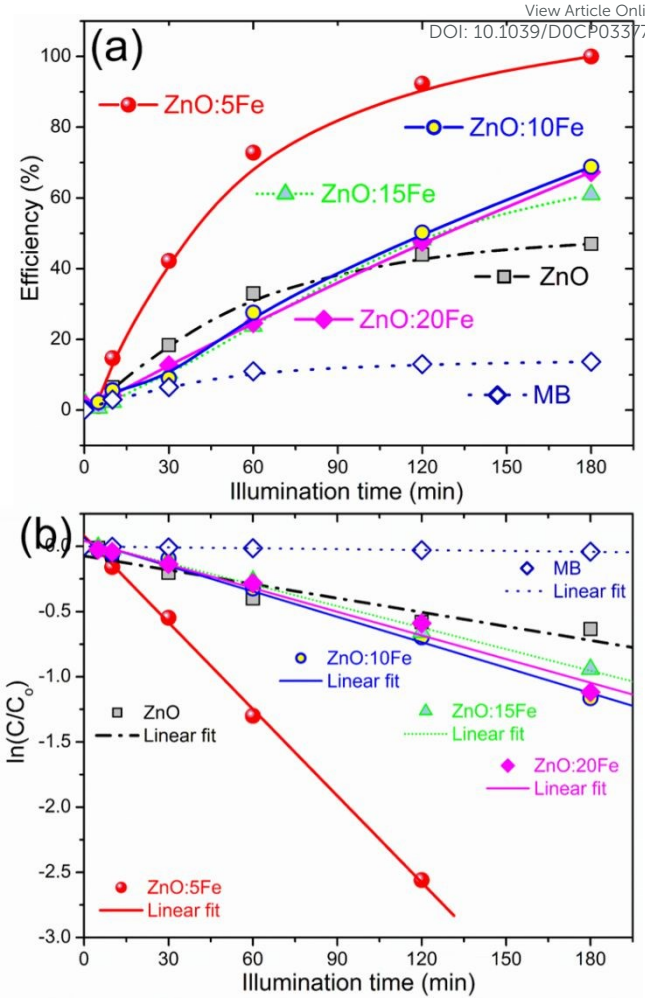

Fig. 11 (a) Photocatalytic efficiency for de-colorization of $[MB]_i$ = 10 ppm in the presence of the ZnO:Fe particles under natural sunlight illumination, and (b) first-order reaction kinetic plots derived from data presented in (a).

Table 5 Kinetic parameters for the photocatalytic de-colorization of MB dye in the presence of ZnO:Fe.

Sample	K_1 (min^{-1})	$t_{1/2}$ (min)
Blank probe	2.23×10^{-4}	3046.6
ZnO	3.60×10^{-3}	192.0
ZnO:5Fe	2.22×10^{-2}	31.3
ZnO:10Fe	6.50×10^{-3}	106.6
ZnO:15Fe	5.50×10^{-3}	126.0
ZnO:20Fe	6.04×10^{-3}	114.6

a certain amount of plate-like particles with the average size of 190 nm, which enhanced the absorption capacity of ZnO for visible light.[25] Besides, the Fe amount decreases the total amount of surface oxygen vacancies (O 1s (2) revealed by XPS, Table 2) and the concentration of bulk oxygen vacancies (according to the results of PL emission spectroscopy).

The results of photocatalytic efficiency are not presented here to promote ZnO:Fe samples as the most efficient photocatalysts. The main intention is to show that among crystal structure, particle size and shape, specific surface area, surface chemistry, electronic– and band–structure, as parameters crucial for photocatalytic activity, particles morphology and optimal surface-to-bulk oxygen vacancy ratio are dominant.

DFT calculations

To investigate the influence of Zn to Fe partial substitution on the electronic structure of ZnO, band structures for all of the investigated cases were calculated along the high-symmetry paths in the Brillouin zone. The calculated band structure of pure ZnO, presented in Fig. 12 (a), is consistent with previous studies[76,77] exhibiting a direct energy gap at the Γ point. Its value is 3.21 eV, in good agreement with the experimental data. Unlike the pure ZnO, all the Fe-doped systems exhibit pronounced spin polarization, i.e. the up and down spins clearly differs. There is no large difference in the calculated band gaps for pure and Fe-doped ZnO, but for the later one the band gap is effectively narrowed as a consequence of formation of isolated states above the valence band maximum, Fig. 12 (b). In the Fe doped system with Zn vacancies, Fig. 12 (c), apart from the states above the valence band maximum, there are additional states also below the conduction band minimum. In the case of the presence of O vacancies, Fig. 12 (d), additional states are not within the band gap, but are merged with valence band maximum, which narrows the band gap noticeably. Large number of bands makes their characterization difficult, so density of states (DOS) plots were also used for in depth analysis.

The total and site-projected densities of states for pure ZnO and Fe-doped ZnO are illustrated in Fig. 13. It can be seen that the overall DOS shapes are in accordance with the previously calculated ones using GGA + U method.[2] For pure ZnO, lower part of the valence band (VB) exhibits narrow peaks, which are mainly composed of the Zn 3d orbitals, while the upper part consists of Zn 3d and O 2p states, which are energetically degenerated and hybridize leading to dispersion of states. The conduction band (CB) has small, gradually increasing DOS, mainly composed of O 2p states. After Fe dopant was introduced in

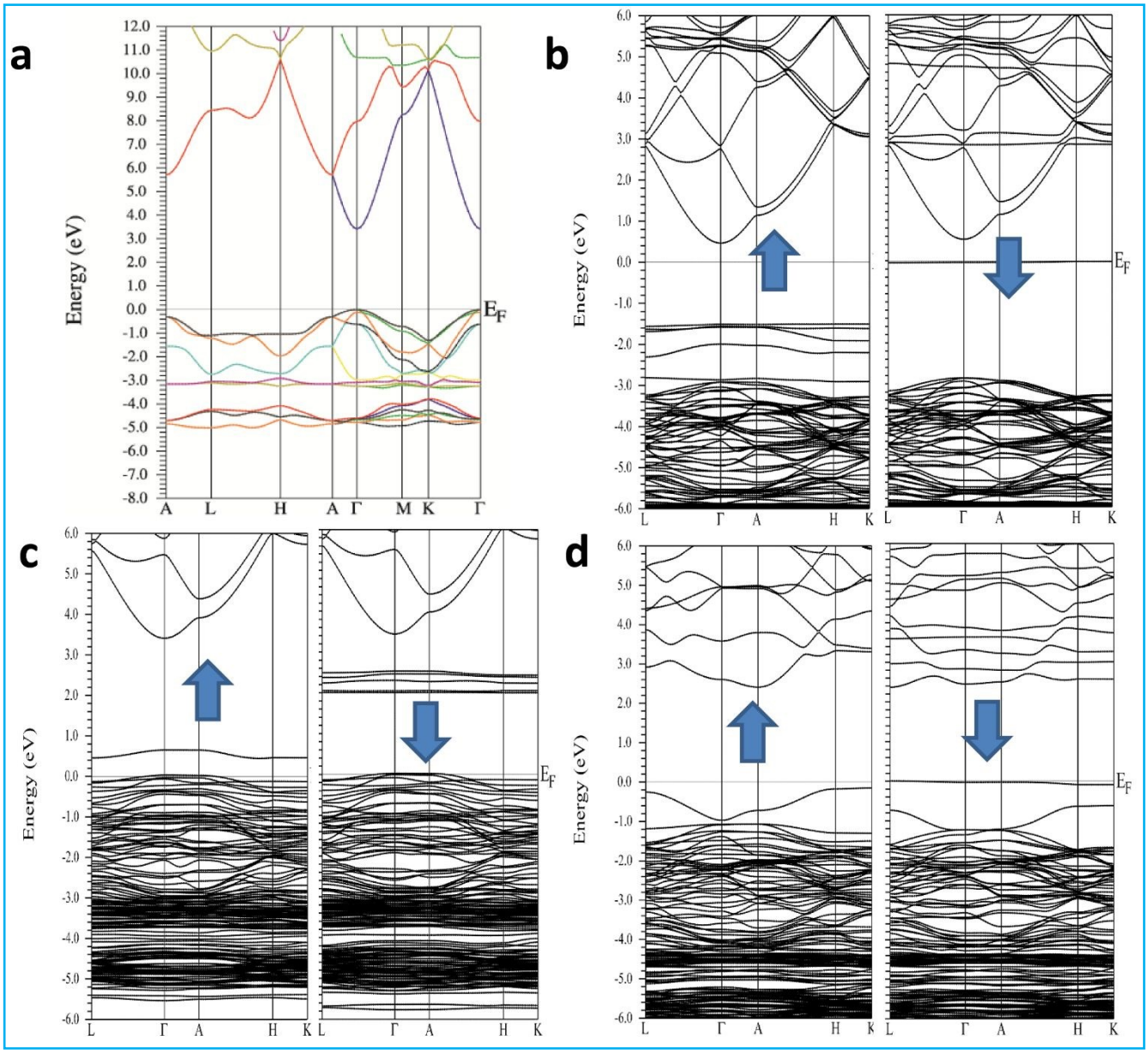

Fig. 12 Calculated band structures of: (a) pure ZnO, (b) Fe-doped ZnO, (c) Fe-doped ZnO with one Zn vacancy in the next nearest neighbour surroundings, and (d) Fe-doped ZnO with one oxygen vacancy in nearest neighbour surroundings. Spin-up and spin-down states are marked by up and down arrows, respectively.

View Article Online
DOI: 10.1039/D0CP03377D

ARTICLE

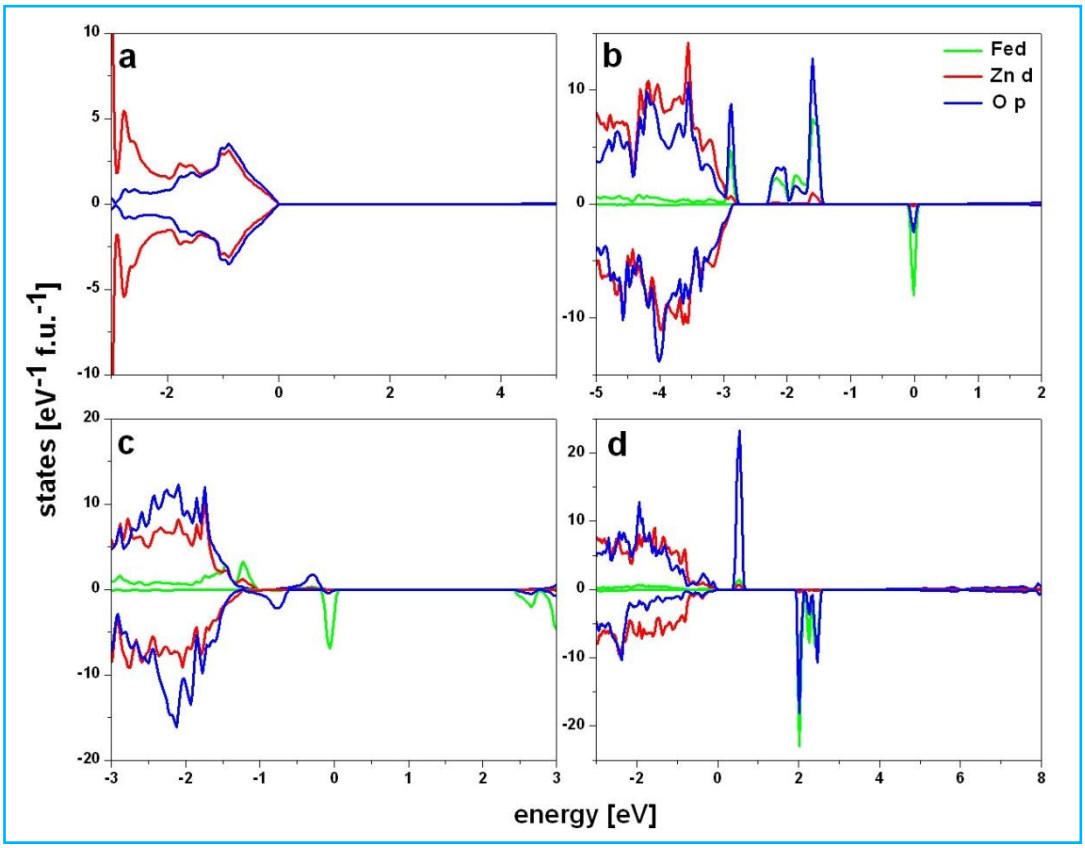

Fig. 13 Density of states for: (a) ZnO, (b) Fe-doped ZnO, (c) Fe-doped ZnO containing O vacancy, and (d) Fe-doped ZnO containing Zn vacancy.

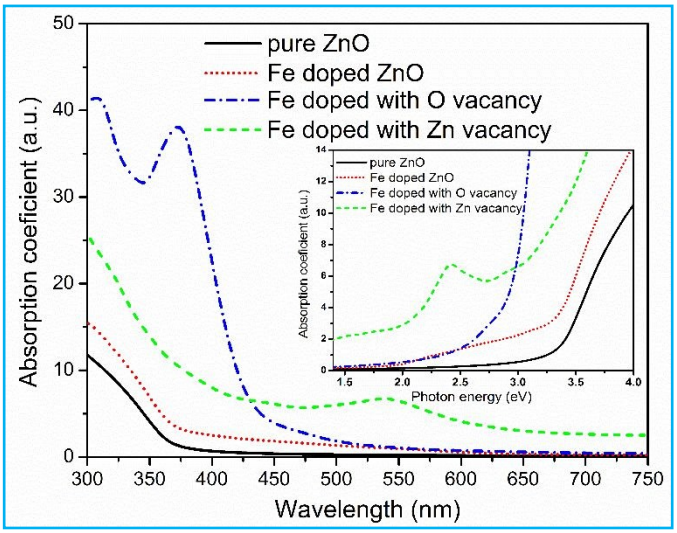

Fig. 14 Optical absorption spectra of pure and Fe-doped ZnO.

the ZnO supercell, impurity states composed mainly of hybridized O p and Fe d states, appear near the VB and CB edges. The situation is similar for the Fe doped system with Zn vacancies. On the contrary, for the Fe doped system with O vacancies, the band gap is narrowed due to the Fe d states that appear at the valence band maximum. Comparing the calculated DOS-es and band gap values with the results obtained from the measurements, we conclude that the situation in our samples corresponds to the Fe doped ZnO without the internal defects in its neighbourhood. This claim is further confirmed by the similarity of the measured (Fig. 7) and calculated (Fig. 14) absorption spectra for the mentioned case. From Fig. 14 can be observed that for all doped systems there is an improvement of the optical absorption in the visible light region as compared with the pure ZnO. The system with O vacancies has the largest absorption in the region up to about 475 nm, while the system with Zn vacancies has the largest extension of the absorption tail into the visible light region.

DOI: 10.1039/D0CP03377D

Conclusions and perspectives

The present study revealed results of detailed physicochemical characterization of ZnO:Fe ($Zn_{1-x}Fe_xO$, $0 \leq x \leq 0.2$) nanoparticles and possibility of their application toward OER and ORR in a moderately alkaline solution. ZnO:Fe nanoparticles were produced by an eco-friendly and rapid microwave irradiation of a precipitate, using low-cost domestic microwave equipment. To comprehend the influence of the partial substitution of Zn^{2+} with Fe^{3+} on the catalytic activity of the ZnO host, phase composition, crystal structure, morphology, textural properties, surface chemistry, optical properties and band-structure were examined. The XRD results reveal that the applied processing conditions can be successfully used for doping concentration up to 15 at.% of Fe, while greater Fe amounts yield a small amount of spinel phase. While XRD results show a hexagonal wurtzite structure, with conserved long-range ordering, Raman spectroscopy confirms that the partial substitution of Zn^{2+} with Fe^{3+} has significantly altered local (short-range) ordering in ZnO, distressing the lattice symmetry. XPS survey spectra confirm the presence of the Fe^{3+} dopant in ZnO:Fe samples, while the HAADF-STEM images with EDS mapping display a homogenous distribution of the dopant throughout ZnO matrix. According to the XPS and PL spectroscopy data, when extra-positively charged Fe^{3+} substitutes Zn^{2+}, the amount of O^{2-} increases, while the density of both surface and bulk oxygen vacancies is reduced. These results are supported by the results of DFT calculations, which suggest that the Fe doped ZnO host without the internal defects in its neighbourhood. The LSV studies show that only ZnO:5Fe has an enhanced catalytic activity toward ORR than pure ZnO, as well as that the activity decreases for the samples with larger Fe amounts. The improved ORR activity of the ZnO:5Fe is indicated by the more positive onset potential (0.394 V *vs*. RHE), current density (0.231 $mA \cdot cm^{-2}$ at 0.150 V *vs*. RHE), and faster kinetics (Tafel slope, b = 248 $mV \cdot dec^{-1}$). The synergy of a sufficient amount of surface oxygen vacancies and a certain amount of plate-like particles results in an improved catalytic activity of the ZnO:5Fe toward ORR. The OER study shows that all Fe-substituted samples have an enhanced activity than pure ZnO. Among them, ZnO:10Fe gives the maximal current density of 1.066 $mA \cdot cm^{-2}$ at 2.216 V *vs*. RHE with the onset potential of 1.856 *vs*. RHE. The smallest potential difference between OER and ORR (ΔE=1.58 V) indicates that ZnO:10Fe could be a promising bifunctional catalysts for OER/ORR in a moderately alkaline solution.

To additionally reduce potential difference between OER and ORR our further study will be focused on $Zn_{1-x}Fe_xO$, $0.05 \leq x \leq 0.1$. We intend to test the OER/ORR activity of ZnO:Fe coupled with different carbon materials, instead pristine ZnO:Fe catalysts, which are presented in this study.

Conflicts of interest

There are no conflicts to declare.

Acknowledgements

This study was financially supported by the Ministry of Education, Science and Technological Development of the Republic of Serbia through the Agreement with the Institute of Technical Sciences of SASA, Grant No. 451-03-68/2020-14/200175, and the Agreement with Vinča Institute of Nuclear Sciences, Grant No. 451-03-68/2020-14/200017, as well as the bilateral cooperation program between the Republic of Serbia and the Republic of Slovenia "Nanostructured and mesoporous functional materials with enhanced solar light driven photocatalytic activity" for 2018–2019. The authors are grateful to Dr. Dijana Đurović from Institute of Public Health of Montenegro, Podgorica, Montenegro, for the ICP-OES analysis.

References

1 I. Kwak, I. S. Kwon, J. Kim, K. Park, J.-P. Ahn, S. J. Yoo, J.-G. Kim and J. Park, *J. Phys. Chem.* C, 2017, **121**, 14899−14906.
2 Y. Lv, W. Yao, X. Ma, C. Pan, R. Zong and Y. Zhu, *Catal. Sci. Technol*., 2013, **3**, 3136–3146.
3 S. Chakrabarty, A. Mukherjee, W.-N. Su and S. Basu, *Int. J. Hydrogen Energy*, 2019, **44**, 1565–1578.
4 J. Pan, X. L. Tian, S. Zaman, Z. Dong, H. Liu, H. S. Park and B. Y. Xia, *Batteries & Supercaps*, 2019, **2**, 336–347.
5 H. Pourfarzad, M. Shabani-Nooshabadi and M. R. Ganjali, *J. Power Sources*, 2020, **451**, 227768.
6 H. Rashid Khan, M. Aamir, B. Akram, A. A. Tahir, M. A. Malik, M. A. Choudhary and J. Akhtar, *Mater. Res. Bull*., 2020, **122**, 110627.
7 Z.-F. Huang, J. Wang, Y. Peng, C.-Y. Jung, A. Fisher and X. Wang, *Adv. Energy Mater*., 2017, **7**, 1700544.
8 Z. Feng, R. Li, Y. Ma, Y. Li, D. Wei, Y. Tang and X. Dai, *Phys. Chem. Chem. Phys*., 2019, **21**, 19651–19659.
9 T. Priamushko, R. Guillet-Nicolas and F. Kleitz, *Inorganics*, 2019, **7**, 9.
10 H.-Y. Su, Y. Gorlin, I. C. Man, F. Calle-Vallejo, J. K. Nørskov, T. F. Jaramillo and J. Rossmeis, *Phys. Chem. Chem. Phys.,* 2012, **14**, 14010–14022.
11 Y. Xu, A. Sumboja, Y. Zong and J. A. Darr, *Catal. Sci. Technol*., 2020, **10**, 2173–2182.
12 M. Shamsuddin, B. Choi and Y.-B. Kim, *Sci. Rep*., 2018, **8**, 2543.
13 S. M. Tan, C. K. Chua, D. Sedmidubský, Z. Sofer and M. Pumera, *Phys. Chem. Chem. Phys.,* 2016, **18**, 1699–1711.
14 C. Chowdhury and A. Datta, *Phys. Chem. Chem. Phys.,* 2018, **20**, 16485–16492.
15 J. Zhu, X. Jiang, Y. Yang, Q. Chen, X.-X. Xue, K. Chen and Y. Feng, *Phys. Chem. Chem. Phys.,* 2019, **21**, 22939–22946.
16 D. Zhang, J. Zhang, L. Gong, Y. Zhu, L. Zhang and Z. Xia, *Phys. Chem. Chem. Phys.,* 2019, **21**, 23094–23101.
17 J.-I. Jung, M. Risch, S. Park, M. G. Kim, G. Nm, H.-Y. Jeong, Y. Shao-Hom and J. Cho, *Energy Environ. Sci*., 2016, **9**, 176–183.
18 J. Masa, W. Xia, I. Sinev, Q. Zhao, Z. Y. Sun, S. Grutzke, P. Weide, M. Mughler and W. Schuhmann, *Angew. Chem. Int. Ed*., 2014, **53**, 8508–8512.
19 M. A. Kirasanova, V. D. Okatenko, D. A. Aksyionov, R. P. Forslund, J. Tyler Mefford, K. J. Stevenson and A. M. Abakumov, *J. Mater. Chem*. A, 2019, **7**, 330–341.
20 D. M. Morales, M. A. Kazakova, S. Dieckhöfer, A. G. Selyutin, G. V. Golubtsov, W. Schuhmann and J. Masa, *Adv. Funct. Mater*., 2020, **30**, 1905992.
21 Y. Sun, Z. Shen, S. Xin, L. Ma, C. Xiao, S. Ding, F. Li and G. Gao, *Electrochim. Acta*, 2017, **224**, 561–570.
22 Md. R. Shakil, A. M. El-Sawy, H. Tasnim, A. G. Meguerdichian,

J. Jin, J. P. Dubrosky and S. L. Suib, *Inorg. Chem*., 2018, **57**, 9977–9987.
23 S. Marković, A. Stanković, J. Dostanić, Lj. Veselinović, L. Mančić, S. D. Škapin, G. Dražić, I. Janković-Častvan and D. Uskoković, *RSC Advances*, 2017, **7**, 42725–42737.
24 S. Marković, V. Rajić, A. Stanković, Lj. Veselinović, J. Belošević-Čavor, K. Batalović, N. Abazović, S. D. Škapin and D. Uskoković, *Sol. Energy*, 2016, **127**, 124–135.
25 S. Marković, I. Stojković Simatović, S. Ahmetović, Lj. Veselinović, S. Stojadinović, V. Rac, S. D. Škapin, D. Bajuk Bogdanović, I. Janković Častvan and D. Uskoković, *RSC Advances*, 2019, **9**, 17165–17178.
26 V. Ivanovski, J. Belošević-Čavor, V. Rajić, A. Umićević, S. Marković, V. Kusigerski, M. Mitrić and V. Koteski, *J. Appl. Phys*., 2019, **126**, 125703.
27 R. Garvey, *Powder Diffr*., 1986, **1**, 114–118.
28 H. P. Klug and L. E. Alexander, "X-ray diffraction procedures for polycrystalline and amorphous materials", Wiley, New York, 4th edn, 1954.
29 F. Rouquerol, J. Rouquerol and K. Sing, "Adsorption by powders and porous solids", Academic Press, London, 1999.
30 E. P. Barrett, L. G. Joyner and P. P. Halenda, *J. Am. Chem. Soc*., 1951, **73**, 373–380.
31 P. Blaha, K. Schwarz, G. K. H. Madsen, D. Kvasnicka and J. Luitz, WIEN 2k an Augmented Plane Wave Plus Local Orbitals Program for Calculating Crystal Properties, Vienna University of Technology, Vienna, Austria, 2001.
32 J. P. Perdew, K. Burke and M. Ernzerhof, *Phys. Rev. Lett*., 1996, **77**, 3865–3868.
33 P. E. Blochl, O. Jepsen and O. K. Andersen, *Phys. Rev. B: Condens. Matter* B, 1994, **49**, 16223–16233.
34 F. Tran and P. Blaha, *Phys. Rev. Lett*., 2009, **102**, 226401.
35 D. B. Melrose and R. J. Stoneham, *J. Phys. A: Math. Gen*., 1977, **10**, L17.
36 S. Heidrun and A. Hans, *J. Appl. Crystallogr*., 2006, **39**, 169–175.
37 E. Solano, C. Frontera, T. Puig, X. Obradors, S. Ricart and J. Ros, *J. Appl. Crystallogr*., 2014, **47**, 414–420.
38 R. D. Shannon, *Acta Cryst*., 1976, **A32**, 751–767.
39 C. A. Arguello, D. L. Rousseau and S. P. S. Porto, *Phys. Rev*., 1969, **181**, 1351–1363.
40 B. Ghosh, S. C. Ray, M. Pontsho, S. Sarma, D. K. Mishra, Y. F. Wang, W. F. Pong and A. M. Strydom, *J. Appl. Phys*., 2018, **123**, 161507.
41 R. Sanchez Zeferino, M. Barboza Flovers and U. Pal, *J. Appl. Phys*., 2011, **109**, 014308.
42 Y. Li, G. Dai, C. Zhou, Q. Zhang, Q. Wan, L. Fu, J. Zhang, R. Liu, C. Cao, A. Pan, Y. Zhang and B. Zou, *Nano Res*., 2010, **3**, 326–338.
43 R. Jothilakshmi, V. Ramakrishnan, R. Thangavel, J. Kumar, A. Saruac and M. Kuball, *J. Raman Spectrosc*., 2009, **40**, 556–561.
44 K. Vojisavljević, M. Šćepanović, T. Srećković, M. Grujić-Brojčin, Z. Branković and G. Branković, *J. Phys.: Condens. Matter*, 2008, **20**, 475202.
45 R. Cuscó, E. Alarcón-Lladó, J. Ibáñez, L. Artús, J. Jiménez, B. Wang and M. J. Callahan, *Phys. Rev. B: Condens. Matter Mater. Phys.*, 2007, **75**, 165202.
46 A. Pimentel, D. Nunes, P. Duarte, V. Rodrigues, F. M. Costa, T. Monteiro, R. Martins and E. Fortunato, *J. Phys. Chem*. C, 2014, **118**, 14629–14639.
47 M. Açıkgöz, M. D. Drahus, A. Ozarowski, J. van Tol, S. Weber and E. Erdem, *J. Phys.: Condens. Matter*, 2014, **26**, 155803.
48 T. Srinivasulu, K. Saritha and K.T. Ramakrishna Redd, *Mod. Electron. Mater*., 2017, **3**, 76–85.
49 T. A. Abdel-Baset, Y.-W. Fang, B. Anis, C.-G. Duan and M. Abdel-Hafiez, *Nanoscale Res. Lett*., 2016, **11**, 115.
50 B. Xu and K. M. Poduska, *Phys. Chem. Chem. Phys*., 2014, **16**, 17634–17639.
51 M. C. Biesinger, B. P. Payne, A. P. Grosvenor, L. W. M. Lau, A. R. Gerson and R. St. C. Smart, *Appl. Surf. Sci*., 2011, **257**, 2717–2730.
52 R. Al-Gaashani, S. Radiman, A. R. Daud, N. Tabet and Y. Al-Douri, *Ceram. Int*., 2013, **39**, 2283–2292.
53 M. C. Biesinger, L. W. M. Lau, A. R. Gerson and R. St. C. Smart, *Appl. Surf. Sci*., 2010, **257**, 887–898.
54 V. Kumar, H. C. Swart, O. M. Ntwaeaborwa, R. E. Kroon, J. J. Terblans, S. K. K. Shaat, A. Yousif and M. M., Duvenhage, *Mater. Lett*., 2013, **101**, 57–60.
55 L. S. Vlasenko, *Appl. Magn. Reson*., 2010, **39**, 103–111.
56 A. Sayari, L. El Mir and H. J. von Bardeleben, *Eur. Phys. J. Appl. Phys*., 2014, **67**, 10401.
57 X.-L. Li, X.-H. Xu, Z.-Y. Quan, J.-F. Guo, H.-S. Wu and G. A. Gehring, *J. Appl. Phys*., 2009, **105**, 103914.
58 N. G. Kakazey, T. V. Sreckovic and M. M. Ristic, *J. Mater. Sci*., 1997, **32**, 4619–4622.
59 A. J. Reddy, M. K. Kokila, H. Nagabhushana, S. C. Sharma, J. L. Rao, C. Shivakumara, B. M. Nagabhushana and R. P. S. Chakradhar, *Mater. Chem. Phys*., 2012, **133**, 876–883.
60 R. Kumar Singh and A. Srinivasan, *J. Magn. Magn. Mater*., 2010, **322**, 2018–2022.
61 S. K. S. Parashar, B. S. Murty, S. Repp, S. Weber and E. Erdem, *J. Appl. Phys*., 2012, **111**, 113712.
62 S. Polarz, *Adv. Funct. Mater*., 2011, **21**, 3214–3230.
63 T. Andelman, Y. Y. Gong, M. Polking, M. Yin, I. Kuskovsky, G. Neumark and S. O'Brien, *J. Phys. Chem*. *B*, 2005, **109**, 14314–14318.
64 D. Flak, A. Braun, A. Vollmer and M. Rekas, *Sens. Actuators* B, 2013, **187**, 347–355.
65 N. S. Han, H. S. Shim, J. H. Seo, S. Y. Kim, S. M. Park and J. K.Song, *J. Appl. Phys*., 2010, **107**, 084306.
66 W. Yang, B. Zhang, Q. Zhang, L. Wang, B. Song, Y. Ding and C. P. Wong, *RSC Adv*., 2017, **7**, 11345–11354.
67 J.A. Navıo, G. Colón, M. Macıas, C. Real and M. I. Litter, *Appl. Catal. A: General*, 1999, **177**, 111–120.
68 K. J. Kim and Y. R. Park, *J. Appl. Phys*., 2004, **96**, 4150.
69 H. Zeng, G. Duan, Y. Li, S. Yang, X. Xu and W. Cai, *Adv. Funct. Mater*., 2010, **20**, 561–572.
70 N. H. Alvi, K. ul Hasan, O. Nur and M. Willander, *Nanoscale Res. Lett*., 2011, **6**, 130.
71 B. Jin and D. Wang, *J. Lumin*., 2012, **132**, 1879–1884.
72 C. H. Ahn, Y. Y. Kim, D. C. Kim, S. K. Mohanta and H. K. Cho, *J. Appl. Phys*., 2009, **105**, 013502.
73 X. Li, C. Gao, J. Wang, B. Lu, W. Chen, J. Song, S. Zhang, Z. Zhang, X. Pan and E. Xie, *J. Power Sources*, 2012, **214**, 244–250.
74 S. K. Bikkarolla, P. Cumpson, P. Joseph and P. Papakonstantinou, *Faraday Discuss*., 2014, **173**, 415–428.
75 H. Zhou, Y. Shi, Q. Dong, J. Lin, A. Wang and T. Ma, *J. Phys. Chem.* C, 2014, **118**, 20100–20106.
76 D. J. Singh, *Phys. Rev. B: Condens. Matter*, 2010, **82**, 205102.
77 R. Vidya, P. Ravindran, H. Fjellvag, B. G. Svensson, E. Monakhov, M. Ganchenkova and R. M. Nieminen, *Phys. Rev. B: Condens. Matter*, 2011, **83**, 045206.

View Article Online
DOI: 10.1039/D0CP03377D

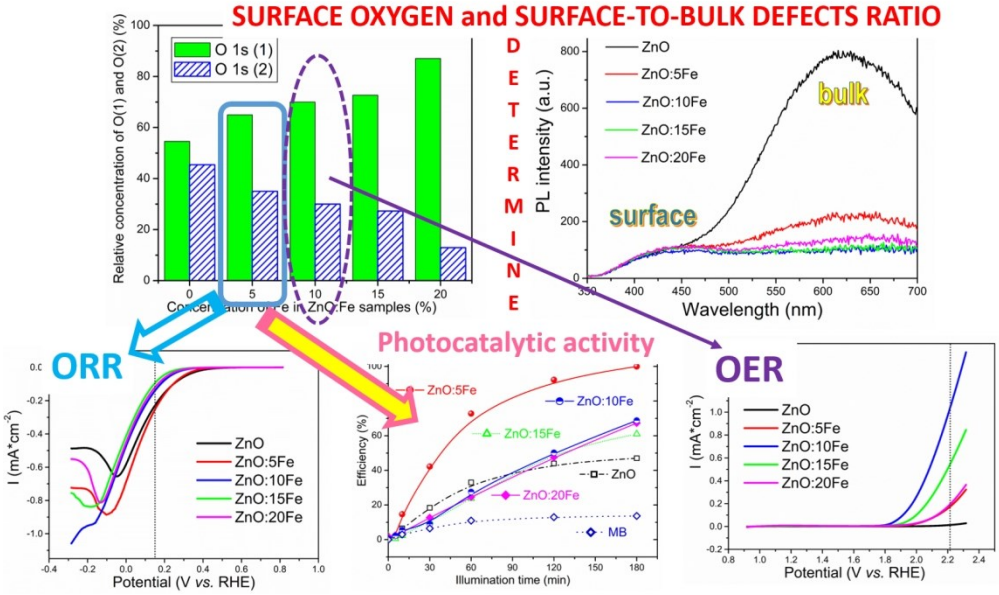

Graphical abstract

439x266mm (96 x 96 DPI)